UC Irvine
UC Irvine Previously Published Works

Title

Radial pair correlation of molecular brightness fluctuations maps protein diffusion as a function of oligomeric state within live-cell nuclear architecture

Permalink

Journal

ISSN

Authors

Solano, Ashleigh
Lou, Jieqiong
Scipioni, Lorenzo
et al.

Publication Date

DOI

Radial pair correlation of molecular brightness fluctuations maps protein diffusion as a function of oligomeric state within live-cell nuclear architecture

Ashleigh Solano,[1,2] Jieqiong Lou,[1,2] Lorenzo Scipioni,[3] Enrico Gratton,[3,*] and Elizabeth Hinde[1,2,*]
[1]School of Physics, University of Melbourne; [2]Department of Biochemistry and Pharmacology, University of Melbourne; and [3]Department of Biomedical Engineering, University of California, Irvine

ABSTRACT Nuclear proteins can modulate their DNA binding activity and the exploration volume available during DNA target search by self-associating into higher-order oligomers. Directly tracking this process in the nucleoplasm of a living cell is, however, a complex task. Thus, here we present a microscopy method based on radial pair correlation of molecular brightness fluctuations (radial pCOMB) that can extract the mobility of a fluorescently tagged nuclear protein as a function of its oligomeric state and spatiotemporally map the anisotropy of this parameter with respect to nuclear architecture. By simply performing a rapid frame scan acquisition, radial pCOMB has the capacity to detect, within each pixel, protein oligomer formation and the size-dependent obstruction nuclear architecture imparts on this complex's transport across sub-micrometer distances. From application of radial pCOMB to an oligomeric transcription factor and DNA repair protein, we demonstrate that homo-oligomer formation differentially regulates chromatin accessibility and interaction with the DNA template.

SIGNIFICANCE Biological proteins self-associate into dimers and higher-order oligomers as a means to modulate their diffusive route throughout the intracellular landscape and modify interaction with target ligands. Currently it is not possible to spatiotemporally track this process in a living cell. Thus, here we present a microscopy method to detect a fluorescently tagged protein of interest undergoing oligomer formation and spatially map the impact intracellular architecture has on this complex's transport across sub-micrometer distances as a function of time. This method is based on radial pair correlation of molecular brightness fluctuations, and we demonstrate that this biophysical tool has the capacity to be an invaluable asset for cell biologists who want to investigate nuclear protein traffic and DNA target search.

INTRODUCTION

Nuclear architecture is fundamental to the manner by which transcription factors (TFs) diffuse throughout the nucleus to reach a target DNA sequence (1–4). In the crowded environment of the nucleoplasm, dynamic rearrangements in chromatin compaction locally redefine the space accessible for TF exploration and this in turn modulates local TF concentration as well as the DNA sequences available for TF interaction (5–9). The spatial heterogeneity in TF localization imparted by the chromatin network, coupled with the sequence specificity of a TF's DNA binding domain (DBD), is what governs the functional output of nuclear wide DNA-TF interactions in a living cell (10–12). Intrigu-

ingly, within this complex framework, a subset of TFs employ oligomer formation to execute entirely distinct expression programs (13). The exact mechanism by which the different oligomeric states of a single TF achieve different functional outputs within a single cell remains unknown.

In vitro binding assays and chromatin immunoprecipitation (ChIP) sequencing (12), as well as different approaches to live-cell microscopy of protein-protein interaction (14–19), have collectively shown that TF oligomer formation alters local DNA binding affinity and sequence specificity. An overlooked repercussion of TF oligomer formation is, however, the reduction in exploration volume that an increase in TF size might impart on DNA target search dynamics. For example, since the DNA network mesh size is comparable with the hydrodynamic radii of many globular proteins (5,6,8,20), depending on when and where a TF monomer dimerizes or undergoes a dimer-tetramer transition during DNA target search, an increase in hydrodynamic radius

may modify a TF's diffusive route and the DNA density threshold that restricts access to specific genomic locations. Thus, here we hypothesize that TF oligomer formation modulates the exploration volume available during DNA target search as a means to differentially control where a TF can interact with the genome. To measure this in a living cell, here we establish a microscopy method to spatially map TF lateral diffusion as a function of oligomeric state within nuclear architecture.

TF oligomerization in live cells can be quantified by coupling confocal microscopy with a specific variant of fluorescence fluctuation spectroscopy (FFS) called moment analysis (4,20–22). Typically, this type of microscopy experiment involves the acquisition of temporal fluctuations in fluorescent intensity due to a fluorescent protein's intracellular dynamics, and then calculation of the acquired fluorescence fluctuations' variance (second moment) normalized with the mean (first moment), to obtain the moving fluorescent protein's apparent brightness, which can be directly translated to its oligomeric state (23–26). In this simplest case, where just a first- versus second-order moment analysis is applied to a fluorescent protein's intensity fluctuations, the average number of sub-units within an oligomeric TF complex is extracted (27). After this, to interrogate the co-existence of different oligomeric species, either a higher-order moment analysis of the temporal fluorescence fluctuations at a single point is performed (28–30) or the ensemble molecular brightness of the TF within each pixel of a confocal frame acquisition is mapped and TF oligomer spatial heterogeneity is explored (31–35). However, while both approaches are invaluable at detecting heterogeneity in TF oligomerization throughout a living cell, neither report on how the different TF oligomeric states modulate TF transport in the nucleus or the kinetics of TF DNA binding activity.

Extensive insight into the mechanisms that underpin TF DNA target search in a living cell has been gained from single particle tracking (SPT) (36–40). However, while SPT has very high spatial resolution when recovering the exploration volume of a single particle, this method is not sensitive toward TF oligomer formation. Thus, we recently combined the capacity of another FFS-based approach, termed pair correlation function (pCF) analysis, to track molecular flow along a confocal line scan (7,41,42), with a moment-based detection of TF oligomeric events (20). This method, termed pair correlation of molecular brightness (pCOMB), measures TF translocation as a function of oligomeric state by amplifying the signal from the brightest species present and sorting extracted oligomer dynamics based on arrival time between two locations (20). pCOMB is effective because TF complex formation modulates DNA binding affinity (13) and interaction with DNA prevents spatial translocation (43). However, since to date pCOMB is performed between a pair of points along a one-dimensional line scan, oligomer-induced changes in TF mobility

are only assessed temporally and assumed to be isotropic. Thus, the impact TF oligomer formation has on mobility spatially within nuclear architecture remains unexplored.

To extract and spatially map the impact TF complex formation has on the accessibility of the nuclear landscape during DNA target search, here we propose a new method termed radial pCOMB. Radial pCOMB is based on a two-dimensional (2D) frame scan data acquisition and it enables anisotropic TF mobility to be detected and quantified (Fig. 1). In brief, the intensity fluctuations that arise due to a fluorescently labeled TF's mobility in each pixel of a 2D frame scan (Figs. 1 a–c), are first transformed into brightness fluctuations (Figs. 1 d and e) and filtered into a multichannel time series of brightness frames (Fig. 1 f), weighted to record TF monomer, dimer, and oligomer dynamics (Fig. 1 g). Then, successively, a 2D pCF algorithm (44) is applied to each channel of the brightness time series such that the derived brightness fluctuations are radially cross correlated with surrounding brightness fluctuations at a defined distance (Fig. 1 h), and a polar plot reporting the temporal evolution of TF monomer, dimer, and oligomer localization is recovered in each pixel (Fig. 1 i). Collectively, radial pCOMB returns a three-dimensional (3D) matrix of spatiotemporal correlation functions that track TF mobility as a function of oligomeric state across different spatial scales. Coupled with a moment-based analysis to assess 2D-pCF polar plot geometry (45,46) (Fig. 1 j), radial pCOMB also has the potential to map where TF mobility is anisotropic (Fig 1 k), and thus detect the impact of nuclear architecture (chromatin) on DNA target search.

To establish radial pCOMB as a method to quantify the spatiotemporal dynamics of an oligomeric TF during DNA target search, we first developed a workflow of brightness fluctuation analysis that can dissect the diffusive route a heterogeneous population of oligomers adopts within nuclear architecture and then applied it to confocal microscopy data acquired in live cells co-expressing different sized multimers of eGFP (monomers, dimers, and pentamers). This pilot experiment, together with simulations, demonstrated that when radial pCOMB is applied to a low-density population (<100 nM) of mobile particles labeled with a fluorophore as bright as eGFP ($\sim25{,}000$ cs^{-1}m^{-1}), this method is sensitive to the size-dependent obstruction nuclear architecture imparts on protein transport across sub-micrometer distances, provided the spatiotemporal resolution and statistics of the microscopy data acquisition employed are optimized. Thus, we then tested the capacity of radial pCOMB to extract the impact of nuclear architecture on the DNA target search strategy of two different oligomeric nuclear proteins labeled with eGFP, our biological application of interest; specifically, an eGFP-labeled construct of the signal transducer and activator of transcription 3 (STAT3-eGFP) that is reported to undergo a dimer to tetramer transition upon activation (20,47–49), and the tumor suppressor p53-binding protein 1 (eGFP-53BP1) that acts as a dimer during
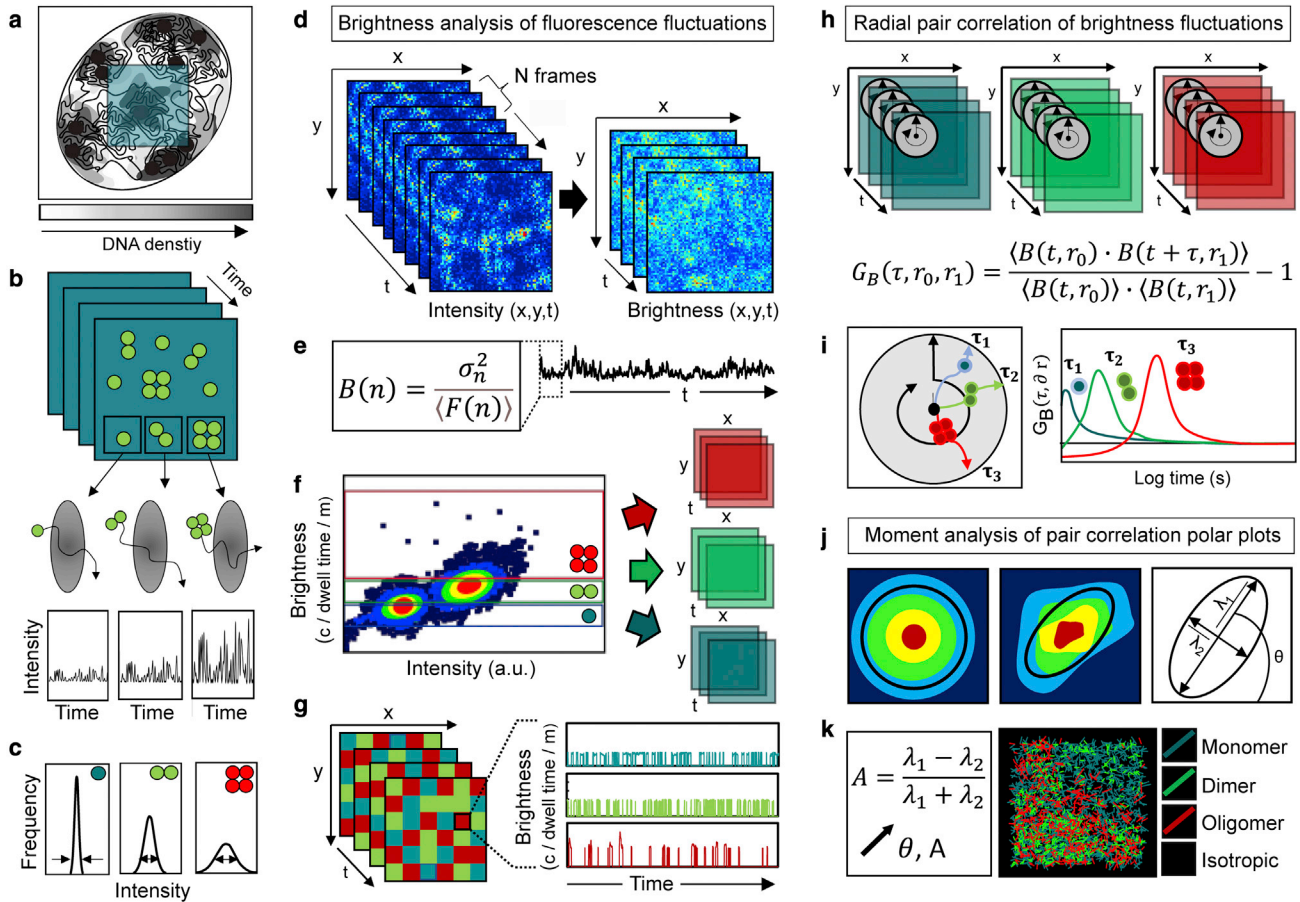
FIGURE 1 Radial pair correlation of molecular brightness (pCOMB) fluctuations. (*a–c*) Principle behind brightness analysis. (*a*) Schematic of a region of interest (ROI) selected for radial pCOMB analysis inside the nucleus of a cell. (*b*) 2D frame scan acquisition of the ROI selected in (*a*) that contains, in each pixel, fluctuations in nuclear protein fluorescence intensity that report the dynamics of this population navigating nucleus architecture as a function of oligomeric state. (*c*) The fluctuations in nuclear protein fluorescence intensity recorded in (*b*) exhibit a variance with respect to the mean that is indicative of nuclear protein brightness– a parameter that can be translated to nuclear protein oligomeric state. (*d–e*) Deriving a time series of brightness frames. (*d*) Schematic of a 2D frame scan acquisition of intensity frames being transformed into a time series of brightness frames via use of a sliding window of moment-based brightness analysis. (*e*) The sliding window of moment analysis used in (*d*) involves calculating the variance σ_n^2 of each pixel's fluctuations in fluorescence intensity normalized to the mean $\langle F(n) \rangle$ across a temporal segment (N frames) that is incrementally shifted to produce a time series of brightness values B(n). The unit of B is counts per pixel dwell time per molecule (c/dwell time/m). (*f–g*) Splitting brightness movie. (*f*) Schematic of how the distribution of brightness values recorded in each pixel of a time series of brightness frames can be filtered into channels weighted to record nuclear protein monomer, dimer, and higher-order oligomer spatiotemporal dynamics (filter is based on independent calibration of the monomer brightness). (*g*) In each pixel of the filtered brightness movie in (*f*), fluctuations in nuclear protein monomer, dimer, and higher-order oligomer brightness are recovered that are indicative of these different species' mobility. (*h-i*) Radial pCOMB analysis of a filtered brightness movie. (*h*) Schematic of the radial pair correlation function $G_B(\tau, r_0, r_1)$ being applied to the nuclear protein brightness fluctuations recorded in each pixel of the split brightness movie (teal = monomer, green = dimer, and red = higher-order oligomer) at a set radius δr in 32 distinct angles. (*i*) The radial pCOMB function defined in (*h*) returns a polar plot in each pixel of each channel that, when collapsed into a single pair correlation profile, per channel, reports the average arrival time of the nuclear protein as a function of oligomeric state (but independent of direction). (*j–k*) Moment analysis of radial pCOMB geometry. (*j*) Moment analysis of the radial pCOMB polar plot geometry in each pixel of each channel detects where nuclear protein mobility is isotropic versus anisotropic. (*k*) The anisotropy *A* and preferential angle of motion *θ* quantified in each pixel of each channel can be used to generate a map of connectivity that visualizes where nuclear protein diffusion is obstructed as a function of oligomeric state. To see this figure in color, go online.

DNA repair and self-associates into higher-order oligomers at DNA double strand break (DSB) sites (50,51). These biological experiments, alongside our baseline radial pCOMB study of eGFP monomers, dimers, and pentamers, demonstrate that homo-oligomer formation does appear to refine the DNA target search strategy of a nuclear protein by making the nuclear landscape less accessible and differentially regulating affinity for the DNA template.

METHODS

Simulations

To explore the potential of radial pCOMB to track fluorescent protein oligomer mobility in silico, a 3.2-μm square box filled with 2000 particles exhibiting different molecular brightness ε values that could freely diffuse along the confinement of an x-y plane was set up to mimic a heterogeneous fluorescent protein oligomer population in a living cell. The composition set for the 2000 particles was a 50:40:10 fraction ratio of monomers

($\varepsilon_{monomer}$ = 100000 cs^{-1}m^{-1}), dimers (ε_{dimer} = 200000 cs^{-1}m^{-1}), and pentamers ($\varepsilon_{pentamer}$ = 500000 cs^{-1}m^{-1}) to reflect the fact that, in the cellular environment, the monomeric population is often significantly abundant over the higher-order oligomeric states, and the different sized fluorescent protein oligomers were assigned distinct diffusion coefficients (D$_{monomer}$ = 1.0 μm^2 s^{-1}, D$_{dimer}$ = 0.5 μm^2 s^{-1}, D$_{pentamer}$ = 0.1 μm^2 s^{-1}) to reflect the expectation that an increase in molecular size results in a reduction in mobility. A 32-pixel grid raster scan was performed across the box filled with particles using a 3D gaussian point spread function (PSF) (with a radial waist of 0.25 μm and axial waist of 1.5 μm) and an 8-μs pixel dwell time, which collectively resulted in an 8-ms frame time (i.e., ~125 frames/s). Once the end of the grid was reached, the PSF returned to the initial starting pixel and this process was reiterated for a total of 8000 frames to derive a 32 × 32 × 8000 image sequence. As a control, this simulation was rerun on a homogenous composition of the monomers, dimers, or pentamers by setting all 2000 particles to exhibit the ε value and diffusion coefficient designated to each of these species in the heterogeneous simulation.

To then examine the impact particle parameters known to affect FFS have on radial pCOMB performance, the heterogeneous and homogenous simulations described above were rerun using different particle densities and ε values. Specifically, to explore particle density, we changed the number of particles in the 3.2-μm square box from 2000 particles to 200 particles (low density) versus 20,000 particles (high density), while maintaining the fraction ratio of monomers, dimers, and pentamers in the heterogeneous population at 50:40:10, alongside their originally defined ε values and diffusion coefficients. In a 3D setting the low-, medium-, and high-density particle populations are equivalent to a particle concentration of 1 nM, 10 nM, and 100 nM, respectively. Then, to explore molecular brightness, we maintained the number of particles in the 3.2-μm square box at 2000 (medium density) and the fraction ratio of monomers, dimers, and pentamers in the heterogeneous population at 50:40:10, alongside their originally defined diffusion coefficients, while reducing the base monomer ε value from 100000 cs^{-1}m^{-1} (high brightness) to 10,000 cs^{-1}m^{-1} (low brightness) (i.e., $\varepsilon_{monomer}$ = 10000 cs^{-1}m^{-1} , ε_{dimer} = 20000 cs^{-1}m^{-1} and $\varepsilon_{pentamer}$ = 50000 cs^{-1}m^{-1}) versus 25,000 cs^{-1}m^{-1} (medium brightness) (i.e., $\varepsilon_{monomer}$ = 25000 cs^{-1}m^{-1}, ε_{dimer} = 50000 cs^{-1}m^{-1} and $\varepsilon_{pentamer}$ = 125000 cs^{-1}m^{-1}). The medium brightness population is equivalent to the reported molecular brightness of eGFP [52], the fluorescent protein used in all of the live-cell radial pCOMB experiments.

Finally, to investigate the impact of live-cell experimental conditions on radial pCOMB performance, the homogenous and heterogeneous simulations based on 2000 particles of only monomers ($\varepsilon_{monomer}$ = 100000 cs^{-1}m^{-1}, D$_{monomer}$ = 1.0 μm^2 s^{-1}), dimers (ε_{dimer} = 200000 cs^{-1}m^{-1}, D$_{dimer}$ = 0.5 μm^2 s^{-1}), and pentamers ($\varepsilon_{pentamer}$ = 500000 cs^{-1}m^{-1}, D$_{pentamer}$ = 0.1 μm^2 s^{-1}) versus a mixture of these three species, were rerun with (1) the presence of photobleaching (an experimental artifact that would be detrimental for brightness-based analysis of oligomer mobility), (2) obstacles that impart anisotropy (a feature of live-cell architecture that radial pCOMB analysis could potentially sense as a function of a protein's oligomeric state), and (3) a scan frame rate more comparable with our laser scanning microscopy experiment (i.e., takes into account the additional time incorporated by the raster scan laser retrace). In the case of photobleaching, the heterogeneous population was simulated with a fraction ratio of 1:1:1 and a photobleaching event was applied to 10% of the molecules (200 particles) in either the monomer, dimer, or pentamer fraction, which resulted in the equivalent of a monomeric sub-unit (i.e., $\varepsilon_{monomer}$ = 100000 cs^{1}m^{-1}) being removed from each particle with a forward reaction rate of 1/250,000 and a reverse reaction rate that was negligible. In the case of anisotropy, the heterogeneous population was simulated with a fraction ratio of 50:40:10 in the presence of trapping zones (four square masks) where the probability of entering or exiting a trapping zone was set to zero. In the case of a slower scan rate, the heterogeneous population was simulated with a fraction ratio of 50:40:10 and sampled

with a 64- versus 128-pixel grid raster scan while maintaining an 8-μs pixel dwell time, which collectively resulted in a 33-ms (i.e., ~30 frames/s) versus a 131-ms (i.e., ~8 frames/s) frame time. All simulations were generated with SimFCS from the Laboratory for Fluorescence Dynamics.

Sample preparation

The capacity of radial pCOMB to track fluorescent protein oligomer mobility within live-cell intracellular architecture was investigated in HeLa cells and the DSB inducible via AsiSI (DIvA) cell system (originally provided by Gaëlle Legube, LBCMCP, CNRS, Toulouse, France) [53–55] transiently transfected with inert and biologically active fluorescent constructs. Both cell lines were cultured in Dulbecco's modified Eagle's medium (Lonza) supplemented with 10% fetal bovine growth serum (Gibco), 1× Pen-Strep (Lonza), and in the case of DIvA 1 μg/mL puromycin (Thermo Fisher Scientific), at 37°C in 5% CO₂. For live-cell microscopy experiments, HeLa and DIvA cells were plated 24 h before experiments onto 35-mm glass-bottom dishes and transfected or co-transfected with the following plasmids via use of Lipofectamine 3000 according to the manufacturer's protocol: eGFP (Euroscarf), 2eGFP (Euroscarf), 5eGFP (Euroscarf), STAT3-eGFP (Ivan Ng in the laboratory of Marie Bogoyevitch and David Jans), and/or eGFP-53BP1 (Addgene, #60813). For the STAT3-eGFP experiments, HeLa cells were treated with 10 nM Oncostatin M (BioVision) and, for the eGFP-53BP1 experiments, DIvA cells were treated with 300 nM 4-hydroxytamoxifen (4OHT).

Fluorescence microscopy

All live-cell radial pCOMB microscopy experiments were performed on an Olympus FV3000 laser scanning microscope coupled to an ISS A320 Fast FLIM box for fluorescence fluctuation data acquisition. A 60× water-immersion objective (1.2 NA) was used for all experiments and the cells were imaged at 37° in 5% CO$_2$. In both HeLa cells and the DIvA cell system the eGFP-tagged plasmids were excited by a 488-nm solid-state laser diode operated at a low power level (1.1 μW at the objective) and the resulting fluorescence signal was directed through a 405/488/561 dichroic mirror to a photomultiplier detector (H7422P-40 of Hamamatsu) fitted with an eGFP 500/25-nm bandwidth filter. For radial pCOMB data acquisition, a HeLa cell exhibiting a low expression of each eGFP-labeled protein was selected (i.e., <100 nM) and then a rapid time series of frames was acquired in a region of interest (ROI) placed across either the (1) cytoplasm, (2) nuclear envelope, or (3) nucleus, using a high electronic zoom (5.3-μm diameter ROI) and a low pixel frame size (64 × 64 pixels, 83-nm pixel size), to minimize frame scan time and maximize statistics (which is important for the pair correlation analysis [45,46]), while enabling a sufficiently long pixel dwell time (8 μs) that did not significantly reduce the apparent brightness of eGFP (which is important for the brightness analysis [20,31]). These frame scan settings enabled 8000 frames to be acquired with a line time of 1.624 ms and a frame time of 105 ms (~10 frames/s) via use of the ISS VistaVision Software, and, importantly, detection of the different eGFP-labeled proteins' diffusive dynamics. The time series of intensity frames were exported as .bin files and processed by a custom code written in MATLAB that applied, first, a moving average to detrend for cell movement and minor photobleaching (which was kept below 10%), and then a pileup correction for the 20-ns deadtime associated with our detection electronics. Low expression of eGFP-labeled protein within each dataset was checked by a moment-based number (N) analysis [31], and confirmation that the eGFP-labeled protein's dynamics were captured by the frame scan was checked by raster image correlation spectroscopy (RICS) [56]. Both the N and RICS data quality checks were performed in SimFCS from the Laboratory for Fluorescence Dynamics.

Brightness movie calculation

Radial pCOMB data generated via both simulation and live-cell microscopy acquisition resulted in a time series of intensity images (X, Y, T) recording the spatiotemporal dynamics of a population of fluorescent molecules, where X and Y are the spatial dimensions, while T is the temporal dimension (number of frames). In each pixel, our signal recorded is represented by the fluorescence intensity as a function of time $F(t)$, where $t = 1, \ldots, T$ are the sampled temporal points. From $F(t)$ we can compute the variance σ^2 and mean $\langle F(t) \rangle$ via Eqs. 1 and 2:

$$\sigma^2 = \frac{\sum_{i=1}^{T}(F_i - \langle F(t) \rangle)^2}{T} \qquad (1)$$

$$\langle F(t) \rangle = \frac{\sum_{i=1}^{T}F_i}{T} \qquad (2)$$

and these quantities can be combined to obtain apparent brightness B according to Eq. 3 as described in previously published papers (23,27,31).

$$B = \frac{\sigma^2}{\langle F(t) \rangle} \qquad (3)$$

When using the entire temporal signal recorded at each pixel, this transformation results in a single apparent brightness value for the fluorescent molecules diffusing through each given location, and therefore a single apparent brightness image that masks any local temporal evolution in apparent brightness due to oligomer formation, or spatially diffusive behavior in the case of a heterogeneous population of oligomeric states. Thus, here we apply the apparent brightness B transformation in a sliding window fashion according to Eq. 4:

$$B(n) = \frac{\sigma_n^2}{\langle F(n) \rangle} \qquad (4)$$

where $n = t, \ldots, t + N$ and N is the size of the sliding window in time (20). Upon extension of this calculation to every pixel, we obtain a brightness movie $B(x, y, n)$ that records spatiotemporal fluctuations in brightness indicative of underlying fluorescent molecule oligomer dynamics, where $x = 1, \ldots, X$ and $y = 1, \ldots, Y$. Throughout the paper we use a sliding window containing $N = 100$ frames that was shifted by $\delta n = 3$ frames. This resulted in 8000 intensity images becoming 2634 brightness frames. The apparent brightness B of a population of fluorescent molecules is related to their ensemble molecular brightness ε according to Eq. 5:

$$B(x, y, n) = \varepsilon(x, y, n) + 1 \qquad (5)$$

where 1 is the brightness contribution of the photon counting detector. Thus, to translate apparent brightness B values into oligomeric states and filter our brightness movie $B(x, y, n)$ into a multichannel time series weighted to record monomer, dimer, and higher-order oligomer (i.e., > dimer) dynamics we filter our brightness movie into:

$$\begin{cases} \varepsilon_{monomer}(x, y, n) = \varepsilon(x, y, n) < 1.5 * \varepsilon_{monomer,cal} \\ \varepsilon_{dimer}(x, y, n) = 1.5 * \varepsilon_{monomer,cal} < \varepsilon(x, y, n) \\ \qquad\qquad\qquad < 2.5 * \varepsilon_{monomer,cal} \\ \varepsilon_{oligomer}(x, y, n) = \varepsilon(x, y, n) > 2.5 * \varepsilon_{monomer,cal} \end{cases}$$

where the molecular brightness value ε of fluorescent molecules in their monomeric form ($\varepsilon_{monomer,cal}$) must first be independently determined to extrapolate the apparent brightness of dimers and or higher-order oligomers (e.g., trimer, tetramer, pentamer). Throughout the paper, this step gave rise to three separate brightness time series of images for radial pCOMB anal-

ysis corresponding to the monomeric ($\varepsilon_{monomer}$), dimeric (ε_{dimer}), and higher-order oligomeric ($\varepsilon_{oligomer}$) species (the latter is assigned as a pentamer ($\varepsilon_{pentamer}$) in the case of simulated and control experiments). The brightness calculations and filtering processes described here for derivation of multichannel brightness movies recording the dynamics of fluorescent monomers, dimers, and higher-order oligomers was carried out in a custom code written in MATLAB that is available at https://github.com/ehinde/Radial-pCOMB.

Radial pair correlation of molecular brightness fluctuations

The multichannel brightness movies derived from a simulated or microscope-acquired time series of intensity images were then analyzed by the radial pair correlation of molecular brightness function described in Eq. 6 (an adaptation of the 2D pair correlation function) (44).

$$G_B(\tau, r_0, r_1) = \frac{\langle B(t, r_0) \cdot B(t + \tau, r_1) \rangle}{\langle B(t, r_0) \rangle \cdot \langle B(t, r_1) \rangle} - 1 \qquad (6)$$

The dimensions of the brightness matrices consisted of x, y, and n components. The x component represents the horizontal pixel distances and the y component represents vertical pixel distances. The n component gives rise to the temporal dimension and represents the delay times between frames. The 2D pair correlation function cross-correlates the brightness fluctuations at a central point of origin $B(t, r_0)$ with surrounding brightness fluctuations $B(t, r_1)$ at a given radial distance δr in 32 distinct angles along an entire radial circumference. Each brightness fluctuation is truncated to the closest 2^n (i.e., 2048 data points) and fast Fourier transformation (FFT) algorithms are then applied to increase the computational efficiency. This calculation is performed in each channel for all pixels within the brightness image series and thus gives rise to a large array containing 32×32 cells, where the first index describes the angle and the second index 32 log spaced delay times. Throughout the paper, to assess the arrival time of the different brightness species within each channel independent of direction, the 32 pCOMB profiles within each cell were radially averaged and the peak time extracted. The radial pCOMB calculations described here for construction of the 3D matrix of spatiotemporal correlation functions were carried out in the custom MATLAB code available at https://github.com/ehinde/Radial-pCOMB.

Moment analysis of radial pCOMB matrix

A moment-based algorithm was also applied to the 3D matrix of spatiotemporal correlation functions generated from radial pCOMB analysis of multichannel brightness movies, prior to radial averaging, to characterize the geometry of each local radial pCOMB polar plot. This involved treating the radial pCOMB data contained within every 32×32 cell as a sub-image $G(x, y)$ and quantification of this sub-image's zero-, first-, and second-order moments in the x and y direction (indexed p and q) using Eq. 7 (where bars denote spatial averages) (45,46).

$$\mu_{pq} = \sum_x \sum_y (x - \overline{x})^p (y - \overline{y})^q G(x, y) \qquad (7)$$

From these moments, the long axis λ_1 and short axis λ_2 of each local radial pCOMB polar plot was obtained with Eq. 8:

$$\lambda_{1,2} = \frac{\mu_{20} + \mu_{02}}{2} \pm \frac{\sqrt{4\mu_{11}^2 + (\mu_{20} - \mu_{02})^2}}{2} \qquad (8)$$

and used to calculate the degree of anisotropy A experienced by fluorescent molecules passing through each pixel according to Eq. 9.

$$A = \frac{\lambda_1 - \lambda_2}{\lambda_1 + \lambda_2} \tag{9}$$

Anisotropy A is indicative of fluorescent molecule obstruction, while the angle θ of the long axis λ_1 described by Eq. 10 is indicative of the resulting preferential direction of motion.

$$\theta = \frac{1}{2}\arctan\left(\frac{2\mu_{11}}{\mu_{20} - \mu_{02}}\right) \tag{10}$$

Throughout the paper these two metrics (anisotropy A and long axis angle θ) were used to quantify and spatially map the magnitude and direction of anisotropic diffusion in each pixel of each channel of a radial pCOMB dataset via construction of a merged map of fluorescent molecule connectivity (45,46). The moment analysis described here for construction of connectivity maps where line length represents the magnitude of anisotropy, line direction the preferential angle of diffusion, and line color the oligomeric state performing the transit were carried out in the custom MATLAB code available at https://github.com/ehinde/Radial-pCOMB.

RESULTS

Radial pair correlation of simulated brightness fluctuations extracts and spatially maps molecular mobility as a function of oligomeric state

To first develop and validate a workflow for radial pCOMB analysis that can spatiotemporally dissect oligomeric protein mobility, we simulated 2D frame scan microscopy data recording fluctuations in fluorescence intensity that result from the movement of (1) a homogenous population of monomers, dimers, and pentamers undergoing isotropic diffusion; versus (2) a heterogeneous mix of these three different species at a density ratio of 50:40:10 (respectively). The different oligomeric states were defined by assignment of different molecular brightness ε values ($\varepsilon_{monomer} = 100{,}000$ cs^{-1}m^{-1}, $\varepsilon_{dimer} = 200{,}000$ cs^{-1}m^{-1} and $\varepsilon_{pentamer} = 500{,}000$ cs^{-1}m^{-1}) and the different sized protein oligomers were assigned distinct diffusion coefficients ($D_{monomer} = 1.0$ μm^2 s^{-1}, $D_{dimer} = 0.5$ μm^2 s^{-1}, $D_{pentamer} = 0.1$ μm^2 s^{-1}) to reflect the expectation that an increase in molecular size results in a reduction in mobility. The homogenous simulations served as a control to both facilitate brightness-based filtering of the heterogeneous simulation and test radial pCOMB's capacity to recover the distinct mobilities of the different brightness species.

The result of these four simulations was a time series of 8000 intensity frames (Fig. 2 a), which, upon being processed with a sliding window of moment-based brightness analysis (Figs. 1 d and e), produced a time series of 2634 brightness frames (Fig. 2 b). The sliding window of moment analysis involved calculating the variance normalized to the mean within each pixel of the intensity frames across a temporal segment (N = 100) that was incrementally shifted ($\delta n = 3$) to produce a times series of brightness values (N = 2634) (Figs. 1 d and e). Construction of histograms

from the apparent brightness values calculated in each pixel of the homogenous simulations (monomer, dimer, and pentamer) (Fig 2 c, left) enabled definition of brightness filters (Fig. 2 c, right) that split the different sized species present in the homogenous and heterogeneous simulations into a monomeric, dimeric, or pentameric channel (Fig. 2 d). In the case of the heterogeneous simulation, these brightness filters split the brightness frames into a three-channel brightness movie weighted to detect monomer, dimer, and pentamer localization as a function of time (Fig. 2 e). Thus, in each pixel of each channel, we obtain brightness fluctuations that record monomer, dimer, and pentamer dynamics (Fig. 2 f), which, upon radial pCOMB analysis with neighboring pixel brightness fluctuations, should in theory enable recovery of the distinct mobilities assigned to the different sized species.

Radial pCOMB analysis is underpinned by a 2D pCF function which, in this context, cross-correlates brightness fluctuations truncated to the nearest 2^n points (N = 2048) in each pixel of each channel of the split brightness movie with surrounding truncated brightness fluctuations at a set radius δr across 32 distinct angles (θ) and for all possible time delays (τ) (Figs. 1 h and i) (44). Thus, collectively, this calculation gives rise to pCOMB polar plots underpinned by 32 pCOMB profiles in each pixel of the monomer, dimer, and pentamer channel that exhibit peaks indicative of the direction and arrival time of molecular transport to a second location (Figs. 1 j and k). Given the isotropic nature of the four simulations under consideration, here we do not yet consider direction. Instead, we radially average the 32 pCOMB profiles derived for a selected δr in each pixel of each channel and collapse what are pCOMB polar plots into radially averaged pCOMB profiles that report the arrival time τ of monomers versus dimers and pentamers across a set area within the heterogeneous simulation's frame scan. Two different radii ($\delta r = 2$ and 8 pixels) were selected to showcase the capacity of radial pCOMB analysis to recover the distinct mobilities assigned to the different sized species within the heterogeneous simulation (Fig. 2 g). Given the simulated frame scan pixel size (100 nm) versus radial axis of the PSF (250 nm) (see section "methods"), pCOMB2 reports oligomer mobility within an observation volume (Fig. 2 g, left), while pCOMB8 is sufficiently large to track oligomer translocation between two spatially distinct observation volumes and enable the oligomeric species of different mobility to spatiotemporally separate (Fig 2 g, right).

From radial pCOMB2 analysis of the filtered brightness movie (Fig. 2 g, left), we find that, while this correlation radius (200 nm) does not permit space for the different species present to translocate or exhibit a distinct arrival time based on the simulated parameters, the amplitude of the monomer, dimer, and pentamer radial correlation profiles are approximately proportional to the square of the molecular brightness filtered into these different channels. Thus, radial pCOMB selectively amplifies the brightest species
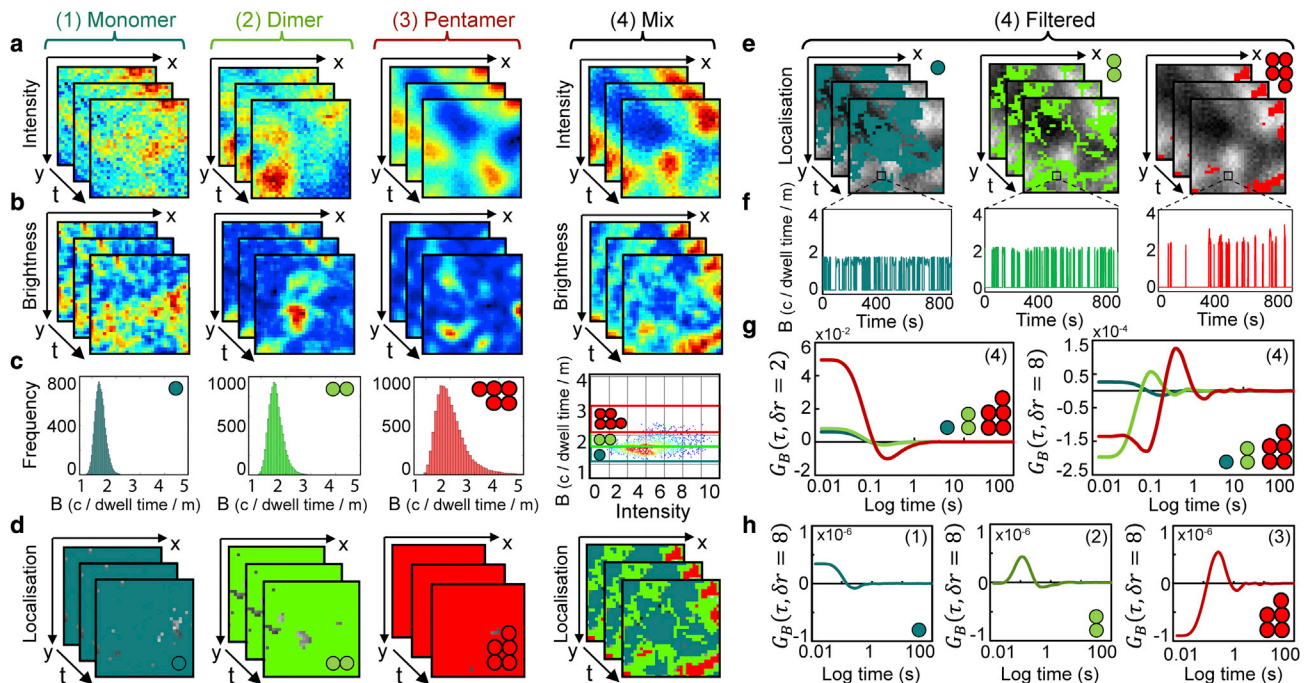
FIGURE 2   Radial pCOMB extracts monomer, dimer, and pentamer spatiotemporal dynamics from a simulated heterogeneous population of particles undergoing isotropic diffusion. (*a*) A simulated 2D frame scan acquisition recording the fluctuations in fluorescence intensity that result from a homogenous (1)–(3) versus heterogeneous (4) population (2000 particles) of monomers ($\varepsilon_{\text{monomer}}$ = 100,000 cs^{-1}m^{-1}, D = 1.0 μm^2 s^{-1}), dimers ($\varepsilon_{\text{dimer}}$ = 200,000 cs^{-1}m^{-1}, D = 0.5 μm^2 s^{-1}), and pentamers ($\varepsilon_{\text{pentamer}}$ = 500,000 cs^{-1}m^{-1}, D = 0.1 μm^2 s^{-1}) undergoing isotropic diffusion. The fraction ratio of the mix is 50:40:10 (respectively). (*b*) Time series of brightness images generated from the simulated times series of intensity images presented in (*a*). (*c*) Brightness histograms (*left*) derived from the homogenous simulations (1)–(3) presented in (*a*) and (*b*) versus a scatter plot of the brightness values (*right*) derived from the heterogeneous simulation (4) presented in (*a*) and (*b*) with superimposed monomer, dimer, and pentamer brightness filters extrapolated from the monomer mean brightness (simulation (1)). (*d*) Time series of the monomer, dimer, and pentamer localization maps that result from splitting the brightness images presented in (*b*) according to the brightness filters defined in (*c*). (*e–f*) Split brightness movie (*e*) of the heterogeneous simulation (4) presented in (*a*) and (*b*) and a zoom in on one pixel's fluctuations in nuclear protein monomer, dimer, and pentamer brightness as a function of time (*f*). (*g*) Average radial pCOMB profiles derived from pair correlation analysis of the heterogeneous simulation (4) split brightness movie presented in (*e*) across a radius of δr = 2 versus 8 pixels (pCOMB2 and pCOMB8). (*h*) Average radial pCOMB8 profiles derived from pair correlation analysis of the homogenous simulation (1)–(3) brightness movies presented in (*d*). To see this figure in color, go online.

present in each channel and this serves as an additional filter for the extraction of dimers and pentamers within their respective channels. From radial pCOMB8 analysis of the filtered brightness movie (Fig. 2 *g*, right) we find, in contrast to pCOMB2, that the larger correlation radius (800 nm) allows space for the different sized oligomeric species to translocate with the simulated parameters and elute at distinct times. Specifically, we recover monomer, dimer, and pentamer correlation profiles with (1) peak positions indicative of an increasingly delayed arrival time, which correctly reflects the mobilities assigned to these different species; and (2) peak amplitudes that imply these different mobility species are indeed different brightness molecules, reflecting the assigned oligomeric states. A comparison of this result (Fig. 2 *g*, right) with radial pCOMB8 analysis of the homogenous simulations (monomer, dimer, and pentamer) (Fig. 2 *h*) confirms this interpretation and demonstrates the capacity of radial pCOMB to accurately extract the mobility of different brightness species within a heterogeneous population.

This radial pCOMB output (Fig. 2 *g*), when evaluated against our previous approach (Fig. S1) that was based on pair correlation analysis of the unfiltered brightness fluctuations (20), reveals that, while selective amplification of the pentamer is maintained in the absence of the brightness filtering (Figs. S1 *a* and *b*), this species' delayed translocation time is not cleanly resolved from the monomers and dimers that are present (Fig. S1 *c*). Specifically, we recover a pCOMB8 profile that is the superimposition of all three species present (Fig. S1 *c*), a result that can be in part rectified by simulating a significant increase in statistics (Fig. S1 *d*). Thus, in the setting of a 2D frame data acquisition where high statistics are not always feasible, the initial brightness filter is critical and offers a more direct solution to data interpretation when the mobilities of the different species present are not sufficiently distinct. In terms of what particle parameters limit the capacity of this brightness filter to assign brightness values recorded within a radial pCOMB acquisition to the correct channel (e.g., monomer versus dimer or higher-order oligomer), we find that they are the

same particle parameters that limit FFS-based brightness analysis in general. In particular, from rerunning the simulations presented in Fig. 2 with different particle densities (Fig. S2), molecular brightness values (Fig. S3), and in the presence of photobleaching (Fig. S4), we find that radial pCOMB performs best on (1) a low- to medium-density population of particles (<100 nM) that are labeled with a fluorescent protein that exhibits a molecular brightness comparable with eGFP ($\sim$25,000 cs^{-1}m^{-1}) (52), since collectively this maximizes the fluctuations in brightness values recorded in each pixel (Figs. S2 and S3), and (2) when the dimer or higher-order oligomer population formed by this monomeric population experiences minimal photobleaching (less than 10%) (Fig. S4).

Finally, to incorporate the directional component of the radial pCOMB function into our workflow of radial pCOMB analysis, we reran the 2D frame scan simulation recording a heterogeneous population of oligomers undergoing isotropic diffusion (Fig. 2), in the absence versus presence of inaccessible obstacles that introduce anisotropy and mimic the crowded environment of a cell (Figs. 3 a–c). Radial pCOMB2 versus pCOMB8 analysis was also applied to these two simulations in each pixel and in each channel across the 32

distinct angles. However, this time, rather than just radially averaging the pCOMB polar plot derived in each pixel of each channel (Figs. 3 d and e), we also performed a moment-based analysis of their individual geometries to identify where and in what direction diffusion is anisotropic when the obstacles are present (Fig. 3 f) (45,46). As can be seen from a comparison of the radially averaged pCOMB8 profiles derived from the two simulations (Figs. 3 g and h), the inaccessible obstacles impart an overall delay to the arrival time of the monomer, dimer, and pentamer, which, in the absence of directional information, is indistinguishable from a scenario where a set of reduced diffusion coefficients is simulated. Thus, to extract the presence of the obstacles, we characterized the angular distribution of the pCOMB polar plot derived in each pixel of each channel by calculation of its central second moment (Fig. 1 j), which gives rise to an ellipse with a major (λ_1) versus minor (λ_2) axis and a major axis angle (θ) (Fig. 1 k). These metrics were then used to quantify the magnitude (normalized ratio between λ_1 and λ_2) and direction (θ) of anisotropic diffusion in each pixel of each channel of each simulation.

As can be seen from comparison of a histogram of the anisotropy values calculated for monomers, dimers, and
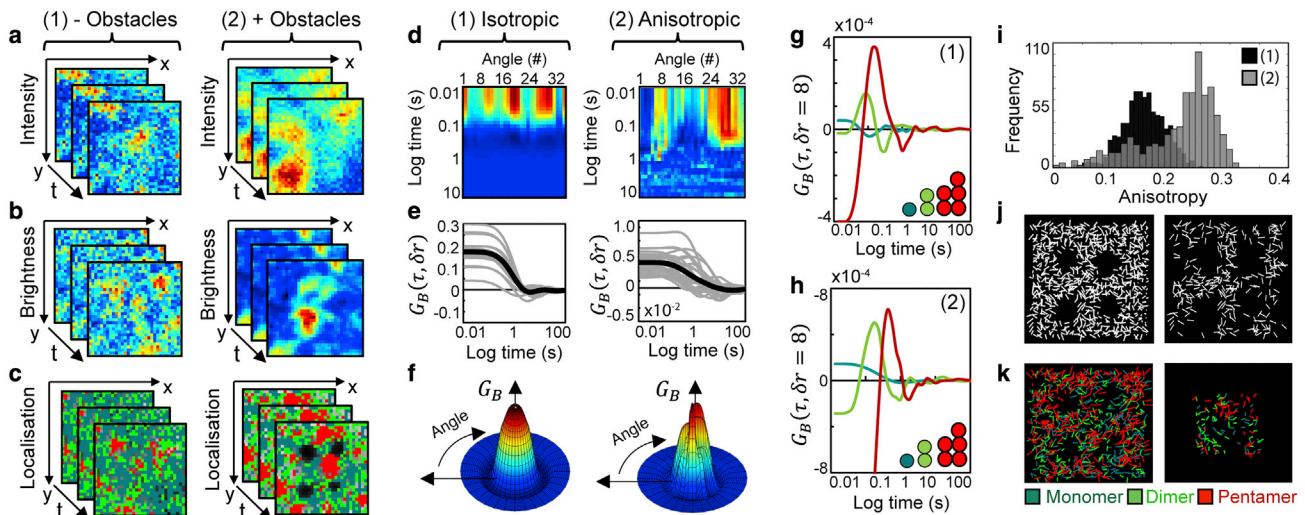

FIGURE 3 Radial pCOMB detects where and in what direction monomer, dimer, and pentamer dynamics are anisotropic from a simulated heterogeneous population of particles undergoing obstructed diffusion. (a) A simulated 2D frame scan acquisition recording the fluctuations in fluorescence intensity that result from a heterogeneous population (2000 particles) of monomers ($\varepsilon_{monomer}$ = 100,000 cs^{-1}m^{-1}, D = 1.0 μm^2 s^{-1}), dimers (ε_{dimer} = 200,000 cs^{-1}m^{-1}, D = 0.5 μm^2 s^{-1}), and pentamers ($\varepsilon_{pentamer}$ = 500,000 cs^{-1}m^{-1}, D = 0.1 μm^2 s^{-1}) (fraction ratio of 50:40:10) undergoing isotropic diffusion in the absence (1) versus presence (2) of inaccessible obstacles. (b–c) Time series of brightness images (b) and split brightness images weighted to record monomer, dimer, and pentamer dynamics (c) that result from the simulated times series of intensity images presented in (a). (d–f) Radial pCOMB analysis of the oligomeric population in (c) across a radius of δr = 2 pixels (pCOMB2) in the absence (simulation (1)) versus presence (simulation (2)) of obstacles (d) and the resulting radially averaged pCOMB2 profiles (e) versus polar plots (f), which are characteristic of isotropic (left) versus anisotropic (right) mobility. (g–h) Average radial pCOMB profiles derived from pair correlation analysis of the heterogeneous simulations' split brightness movie presented in (c) in the absence (simulation (1)) (g) versus presence (simulation (2)) (h) of obstacles across a radius of δr = 8 pixels (pCOMB8). (i) Anisotropy histograms recovered from a moment analysis of the radial pCOMB2 polar plots presented in (f), which were derived from pair correlation analysis of the heterogeneous simulations' split brightness movie in (c) in the absence (simulation (1)) (black) versus presence (simulation (2)) (gray) of obstacles. (j) Maps of connectivity derived from radial pCOMB2 analysis of oligomer mobility in the heterogeneous simulation with obstacles (simulation (2)) in the absence (left) versus presence (right) of an isotropic threshold derived from (i). (k) Merged maps of connectivity derived from radial pCOMB2 (left) versus pCOMB8 (right) analysis of the split brightness movie of the heterogeneous simulation with obstacles (2) presented in (c) report where monomer, dimer, and pentamer mobility is anisotropic. To see this figure in color, go online.

pentamers in the absence (black) versus presence (gray) of obstacles (Fig. 3 *i*), the mean value of anisotropy shifts from 0.17 to 0.28. Thus, to spatially map this obstruction to diffusion within the simulation where obstacles are present, we applied an isotropic threshold (<0.2) to each pixel in each channel and constructed a map of connectivity where each line's length represents the magnitude of anisotropy and its direction the preferential angle of diffusion (Fig. 3 *j*). As can be seen from the merged maps of connectivity derived from pCOMB2 and pCOMB8 analysis of the simulation containing obstacles (Fig. 3 *k*), this data output reports the structural framework being explored by the monomers, dimers, and pentamers. Thus, collectively, radial pCOMB has the capacity to track protein mobility as a function of oligomeric state and map the impact intracellular architecture has on each complex's mode of exploration.

Mapping the accessibility of intracellular architecture by radial pCOMB analysis of different sized eGFP oligomers

To next test radial pCOMB's capacity to report oligomeric protein mobility within an intracellular environment, and define a protocol for the acquisition of fluorescence fluctuation data amenable to this method of analysis, we performed a series of confocal-based microscopy experiments in live HeLa cells transiently transfected with (1) a homogenous population of eGFP monomers (1GFP), dimers (2GFP), or pentamers (5GFP), versus (2) a heterogeneous population of all three species (1GFP, 2GFP, 5GFP). This involved setting up ROIs in the cytoplasm and/or nucleus of HeLa cells individually expressing or co-expressing 1GFP, 2GFP, and 5GFP (Figs. 4 *a* and *b*) at a nanomolar level (i.e., <10 moving particles per pixel) (Figs. S5 *a* and *b*). Then, acquisition of a time series of intensity images within each selected ROI that was spatiotemporally optimized (see section "methods") to capture fluorescence fluctuations originating from movement of the different sized proteins being investigated (Fig. S5 *c*) with minimal photobleaching (<10%, Fig. S5 *d*).

To transform each acquired live-cell fluorescence fluctuation experiment recording 1GFP, 2GFP, and 5GFP dynamics (independently or simultaneously) into a time series of brightness frames, and ultimately a filtered brightness movie, we first applied a moving average to each time series of intensity frames acquired to detrend for photobleaching (Fig. S5 *e*). Then we followed the workflow of radial pCOMB analysis devised from simulation (Figs. 2 and 3). This involved application of the sliding window of moment-based brightness analysis to each pixel of each time series of intensity frames, across a temporal segment that allowed for the dynamics being probed to decay, while maximizing the number of brightness frames generated for subsequent radial pCOMB analysis (Fig. S5 *f*). Then, a brightness histogram was constructed for each time series of brightness frames independently recording 1GFP, 2GFP

or 5GFP dynamics (Fig. 4 *a*), to enable definition of brightness filters to split these different species apart when present within a time series of brightness frames recording 1GFP, 2GFP, and 5GFP dynamics simultaneously (Fig. 4 *b*), and, thus, derivation of a three-channel brightness movie weighted to report monomer, dimer, and pentamer localization as a function of time (Fig. 4 *c*).

To next explore the temporal evolution of eGFP mobility as a function of oligomeric state, independently of direction, within filtered brightness movies recording a heterogeneous population of 1GFP, 2GFP, and 5GFP dynamics throughout intracellular architecture (Figs. 4 *b* and *c*), we first trialed radial pCOMB analysis at a radius of $\delta r = 4$, 6, and 8 pixels (where pCOMB4 = 320 nm, pCOMB6 = 480 nm, and pCOMB8 = 640 nm) (Fig. 4 *d*). As can be seen from the radial average of the pCOMB4, pCOMB6, and pCOMB8 profiles derived for the monomer, dimer, and pentamer channels, the mobility of 1GFP, 2GFP, and 5GFP across the cytoplasm and nucleus was effectively captured from pCOMB4 to pCOMB6; however, beyond this distance range at pCOMB8, only 1GFP and 2GFP transport was detected (Fig 4 *d*). Given that pCOMB8 did not detect 5GFP transport in the pentamer channel, and the pixel size of our frame scan data acquisition (80 nm) results in pCOMB4 favoring local mobility within the radial axis of the laser PSF (∼260 nm), we proceeded with pCOMB6 (480 nm), which ensures detection of 1GFP, 2GFP, and 5GFP transport between distinct observation volumes, a condition that favors spatiotemporal separation of the different sized eGFP species. Interestingly, from calculating the radial average of pCOMB6 across cytoplasmic versus nuclear ROIs defined within filtered brightness movies derived from multiple cells (N = 9), we find that, upon separation of these two sub-cellular compartments, eGFP transport is only differentially regulated as a function of oligomeric state in the nucleus on this spatial scale (Figs. 4 *e* and *f*). Specifically, in the cytoplasm, the different sized eGFP constructs diffuse across the interrogated distance (480 nm) simultaneously on the timescale of the experiment (Fig. 4 *e*), while, in the nucleus, a sequential order to 1GFP (∼0.1 s), 2GFP (∼1.8 s), and 5GFP (∼3.7 s) arrival time is observed in the monomer, dimer, and pentamer channels, respectively (Fig. 4 *f*). Collectively, this result suggests the structural framework of the nucleus represents a size-dependent hindrance to protein transport, a result that was confirmed upon pCOMB6 analysis of the independent 1GFP, 2GFP, and 5GFP experiments (Fig. 4 *a*) in the cytoplasm (Fig. 4 *g*) and nucleus (Fig. 4 *h*).

To next quantify the extent to which obstruction by the nuclear landscape is indeed responsible for the differential regulation of 1GFP, 2GFP, and 5GFP transport across the nucleoplasm, we returned to the pCOMB6 analysis calculated for this sub-cellular ROI prior to radial averaging and applied a moment-based analysis to each pixel's pCOMB6 polar plot. This analysis enabled construction of merged maps of connectivity reporting the anisotropic motion of
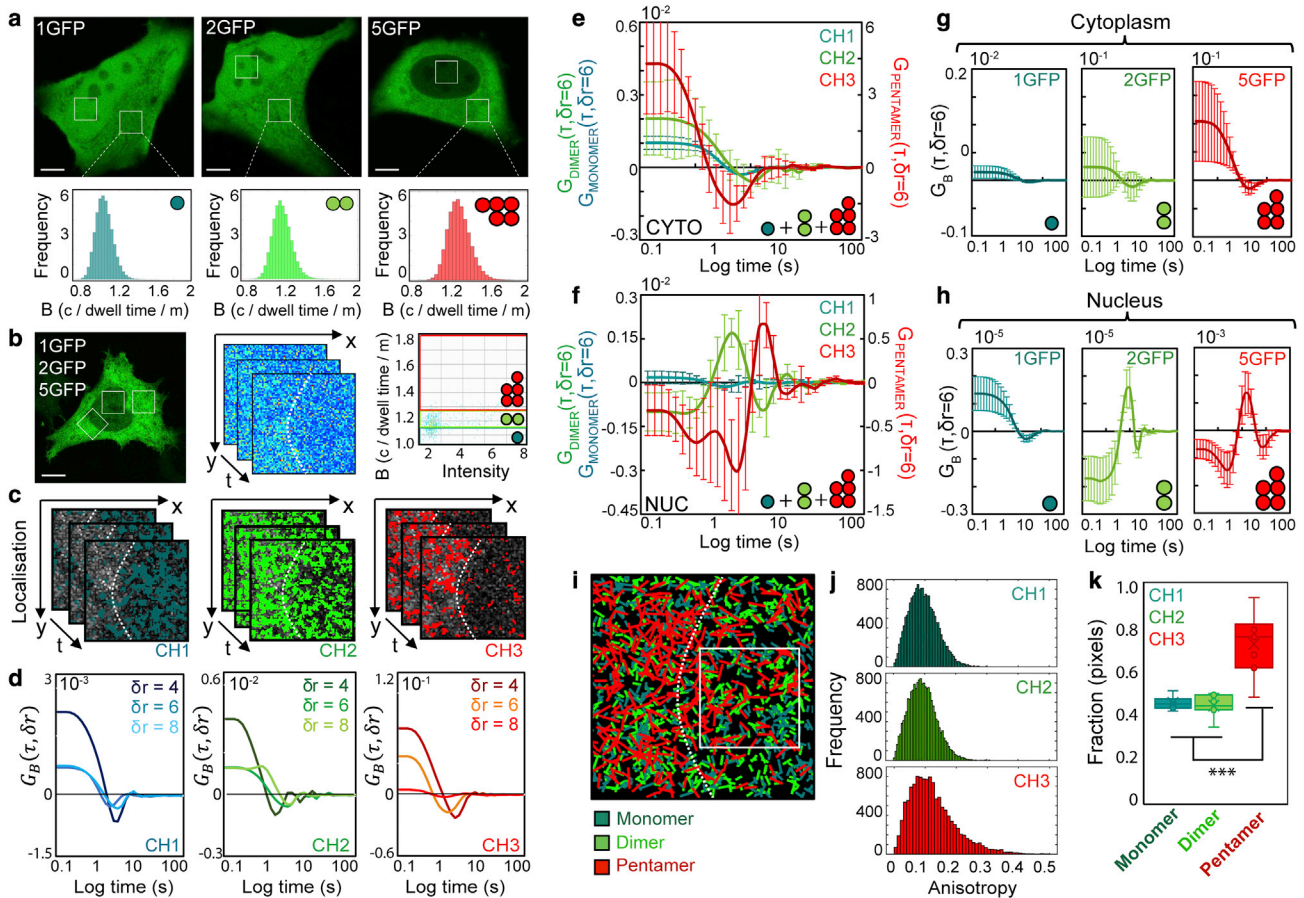
FIGURE 4   Radial pCOMB extracts and spatially maps the spatiotemporal dynamics of eGFP in a living cell as a function of oligomeric state. (*a*) Intensity images of HeLa cells expressing eGFP monomers (1GFP), dimers (2GFP), or pentamers (5GFP), with ROIs selected for radial pCOMB analysis superimposed (*top*), and the histogram of brightness values calculated in the cytoplasmic ROI presented (*bottom*). Scale bar, 5 μm. (*b*) Intensity image of a HeLa cell co-expressing 1GFP, 2GFP, and 5GFP, with ROIs selected for radial pCOMB analysis superimposed (*left*), and the resulting time series of brightness frames calculated from the nuclear envelope ROI (*middle*), alongside a scatterplot of the associated brightness values (*right*), with superimposed brightness filters extrapolated from 1GFP's mean brightness (*a*). Scale bar, 5 μm. (*c*) Split brightness movie of the radial pCOMB acquisition analyzed in (*b*), where channel 1 (CH1), channel 2 (CH2), and channel 3 (CH3) record monomer, dimer, and pentamer dynamics (respectively). (*d*) Radially averaged pCOMB profiles derived from pair correlation analysis of 1GFP, 2GFP, and 5GFP mobility in CH1, CH2, and CH3 of the split brightness movie presented in (*c*) across a radius of $\delta r =$ 4, 6, and 8 pixels (pCOMB4, pCOMB6, and pCOMB8). (*e–f*) Radially averaged pCOMB6 profiles with standard error of the mean for 1GFP, 2GFP, and 5GFP mobility in the cytoplasm (*e*) versus nucleus (*f*) of HeLa cells (N = 9) co-expressing these three species. (*g–h*) Radially averaged pCOMB6 profiles with standard error of the mean for 1GFP, 2GFP, and 5GFP mobility in the cytoplasm (*g*) versus nucleus (*h*) of HeLa cells (N = 5) independently expressing only one of these three species. (*i–j*) Merged map of connectivity (*i*) and anisotropy histograms (*j*) derived from radial pCOMB6 analysis of the split brightness movie presented in (*c*) that report where and to what extent 1GFP, 2GFP, and 5GFP mobility is anisotropic in the selected HeLa cell co-expressing these three species. (*k*) Quantitation of anisotropy histograms constructed from radial pCOMB6 analysis of 1GFP, 2GFP, and 5GFP mobility in the nucleus of HeLa cells (N = 9) co-expressing these three species. Box and whisker plot shows the minimum, maximum, sample median, and first versus third quartiles. ***p $<$ 0.001 (unpaired *t*-tests). To see this figure in color, go online.

eGFP monomers, dimers, and pentamers, which demonstrate a spatial heterogeneity in terms of where each species is obstructed by intracellular architecture (Fig. 4 *i*), as well as calculation of anisotropy histograms reporting the degree of obstruction experienced by each eGFP species within a nuclear ROI (Fig. 4 *j*). As can be seen from a comparison of the derived nuclear anisotropy histograms, and quantitation of the fraction of anisotropic transits detected for 1GFP, 2GFP, and 5GFP across multiple nuclear connectivity maps (N = 6 HeLa cells) (Fig. 4 *k*), we find that 5GFP transport is significantly more obstructed by nucleus architecture

than 1GFP or 2GFP transport. This effect, alongside the size-dependent arrival time of eGFP multimers across submicrometer distances in the nucleoplasm, demonstrates that nuclear protein oligomerization does modulate the exploration volume accessible during DNA target search.

Quantification of nuclear protein oligomer dynamics by radial pCOMB

We next employed radial pCOMB microscopy to quantify the role oligomer formation plays in facilitating DNA target

search strategies in the context of transcription and DNA repair. Specifically, we first applied radial pCOMB to a TF called STAT3, which has been shown to undergo a dimer-tetramer transition upon transcriptional activation by biochemical assays as well as a brightness-based analysis (15,20,47), and then to a DNA repair factor called 53BP1, which has been shown to be dimeric and capable of self-association into higher-order oligomers that exhibit a molecular weight consistent with a tetramer, in response to a DNA double-strand break (DSB) (50,51,57,58).

In the case of STAT3, the impact a dimer-to-tetramer transition has on this TF's nuclear accessibility was investigated by acquisition of radial pCOMB fluorescence fluctuation data in HeLa cells transiently transfected with STAT3-eGFP before and at different time points after treatment with Oncostatin M (OSM). OSM is a cytokine that promotes

STAT3 transcription, and, in the context of HeLa, stimulates STAT3-eGFP to redistribute from the cytoplasm into the nucleus, where it accumulates within 30 min of addition and exhibits reduced mobility (Fig. 5 a and Figs. S6 a and b). Thus, the ROI selected for a time series acquisition of intensity frames reporting STAT3-eGFP dynamics was positioned across the nuclear envelope, acquired under basal (−OSM) (Fig. 5 b, left) versus transcriptionally activated conditions (+OSM) (Fig. 5 c, left), and then transformed into a split brightness movie via use of the filters we defined from independent calibration of the monomeric versus multimeric brightness of eGFP (Figs. 4 a and b). As can be seen from a select set of merged STAT3-eGFP oligomer localization maps taken from the brightness movie acquired 0 to 15 min before (Fig. 5 b, right) and 0 to 15 min after (Fig. 5 c, right) OSM addition, we find that (1)
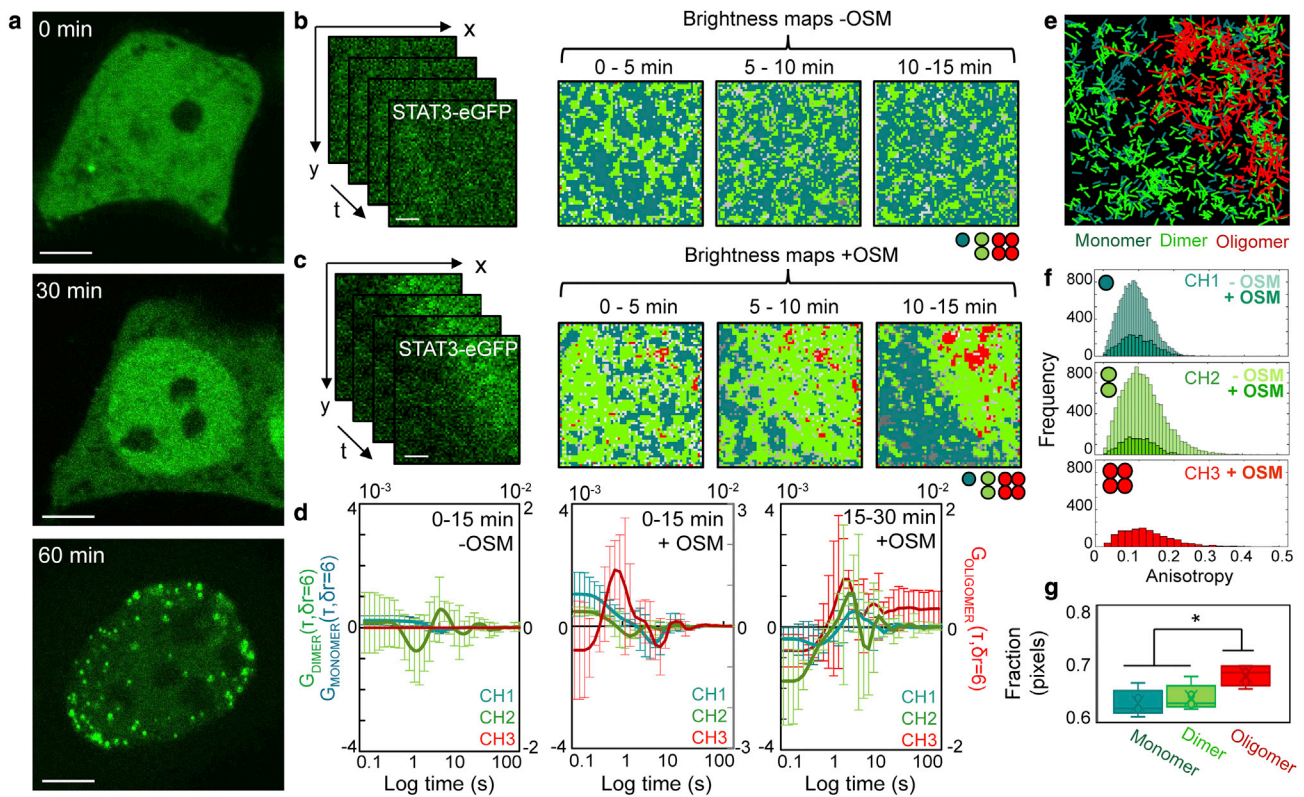

FIGURE 5 Radial pCOMB analysis of STAT3-eGFP oligomer formation and navigation of the nuclear landscape during transcriptional activation. (a) Intensity images of HeLa cells expressing STAT3-eGFP at t = 0 min (top), 30 min (middle), and 60 min (bottom) after treatment with 10 nM Oncostatin M (OSM). Scale bar, 5 μm. (b) Time series of intensity frames within an ROI selected for radial pCOMB analysis prior to OSM treatment (left) and a select set of brightness frames derived from this acquisition that are weighted to record STAT3-eGFP monomers (teal), dimers (green), and higher-order oligomers (e.g., tetramers) (red) (right). Scale bar, 1 μm (c) Time series of intensity frames within an ROI selected for radial pCOMB analysis 15 min after OSM treatment (left) and a select set of brightness frames derived from this acquisition that are weighted to record STAT3-eGFP monomers (teal), dimers (green), and higher-order oligomers (red) (e.g., tetramers) (right). Scale bar, 1 μm. (d) Radially averaged pCOMB profiles with standard error of the mean derived from pair correlation analysis of STAT3-eGFP monomer, dimer, and higher-order oligomer (e.g., tetramers) transport in CH1, CH2, and CH3 of the split brightness movies derived from nuclear ROIs in HeLa cells (N = 4) before versus after OSM treatment (two different time points) across a radius of δr = 6 pixels (pCOMB6). (e–f) Merged map of connectivity (e) and anisotropy histograms (f) derived from radial pCOMB6 analysis of the split brightness movie presented in (c) that report where and to what extent STAT3-eGFP monomer, dimer, and higher-order oligomer (e.g., tetramers) mobility is anisotropic before versus 0–15 min after OSM activation. (g) Quantitation of anisotropy histograms constructed from radial pCOMB6 analysis of STAT3-eGFP monomer, dimer, and higher-order oligomer (e.g., tetramers) mobility in the nucleus of HeLa cells 15–30 min after OSM stimulation (N = 4). Box and whisker plot shows the minimum, maximum, sample median, and first versus third quartiles. *p < 0.05 (unpaired t-tests). To see this figure in color, go online.

STAT3-eGFP monomers (teal) and dimers (green) are detected under basal conditions with no significant spatial redistribution as a function of time, while (2) STAT3-eGFP dimers (green) upon transcriptional activation spatially redistribute from the cytoplasm to the nucleus in parallel to formation of a nuclear higher-order oligomer population (red) (Figs. 5 b, c, and S6 c–e).

To dissect the spatiotemporal dynamics that lead to detection of a nuclear STAT3-eGFP higher-order oligomer population in a HeLa cell, we next performed radial pCOMB analysis at a distance of δr = 6 pixels (480 nm) on each split brightness movie derived from a fluorescence fluctuation dataset acquired 0 to 15 min before OSM treatment, versus 0 to 15 min and 15 to 30 min after OSM treatment. From first calculating the radial average of pCOMB6 across nuclear ROIs defined within the filtered brightness movies derived from multiple cells (N = 4) (Fig. 5 d), we found under basal conditions (−OSM, 0–15 min) that STAT3-eGFP monomers translocate sub-micrometer nuclear distances at a significantly faster rate than STAT3-eGFP dimers ($\tau_{monomer} \sim 0.1$ s versus $\tau_{dimer} \sim 4.7$ s), which agrees with the diffusive behavior of inert eGFP (Fig. 4 f). Then, during the first stage of transcriptional activation (+OSM, 0 to 15 min), when STAT3-eGFP is significantly redistributed from the cytoplasm to the nucleus, we found STAT3-eGFP dimers translocate the nucleoplasm as efficiently as STAT3-eGFP monomers ($\tau_{monomer}$ and $\tau_{dimer} \sim 0.1$ s), in parallel to the formation of a population of STAT3-eGFP higher-order oligomers that exhibit restricted mobility ($\tau_{oligomer} \sim 0.9$ s). Finally, with increasing time after transcriptional activation (+OSM, 15 to 30 min), when an expected increase in STAT3 DNA binding activity is promoted by cytokine stimulation, all three STAT3-eGFP species (monomers, dimers, and higher-order oligomers) experience a significant reduction in mobility that likely reflects the DNA-bound population ($\tau_{monomer}$ and $\tau_{dimer} \sim 2.9$ s versus $\tau_{oligomer} \sim 3.7$ s). Collectively, this result demonstrates that a change in nuclear access coupled with STAT3 self-association (e.g., dimer-tetramer transition) regulates the temporal kinetics of this TF's capacity to scan the genome upon transcriptional activation and, in the end, DNA template interaction.

To next interrogate the impact nuclear access coupled with STAT3-eGFP oligomeric state have on STAT3 spatial mobility, and where this TF can scan or interact with the genome, we returned to the pCOMB6 analysis calculated prior to polar plot radial averaging, and derived (1) connectivity maps reporting the localization of STAT3-eGFP monomer, dimer, and higher-order oligomer anisotropic translocation during transcriptional activation (Figs. 5 e and S6 f–h), as well as (2) anisotropy histograms quantifying the degree of obstruction experienced by each of these species before versus after OSM stimulation (Fig. 5 f). As can be seen from visual inspection of the STAT3-eGFP connectivity map derived after OSM stimulation (Fig. 5 e), nu-

clear STAT3-eGFP dimers experience anisotropy at distinct locations within the nuclear landscape compared with STAT3-eGFP higher-order oligomers, and, while the degree of obstruction experienced by STAT3-eGFP dimers is initially reduced upon transcriptional activation (Fig. 5 f), the fraction of anisotropic transits detected for this species within nuclear ROIs across multiple connectivity maps (N = 4) (Fig. 5 g), is significantly higher than its inert eGFP counterpart (Fig. 4 k). Thus collectively, this result (Figs. 5 e–g and S6 f–h), alongside the observation that STAT3 dimers experience a transient increase in mobility after transcriptional activation (Fig. 5 d), suggests that OSM induces a rearrangement in nucleus architecture that specifically regulates STAT3 dimer access and facilitates STAT3 adopting a nuclear-wide DNA-binding activity that, as a function of oligomeric state, is spatially heterogeneous.

In the case of 53BP1, the effect higher-order oligomer formation has on this DNA repair factor's nuclear access during a DSB DNA damage response (DDR) was investigated by acquisition of radial pCOMB fluorescence fluctuation data in the DSB inducible via AsiSI cell system (DIvA) (54,55) transiently transfected with eGFP-53BP1. DivA cells are a stable cell line generated in the human U2OS background harboring a 4OHT-inducible AsiSI restriction enzyme, which allows for induction of approximately 100 site-specific DSBs in the genome upon 4OHT treatment, and recruitment of nuclear 53BP1 to these nuclear locations (Figs. 6 a, S7 a and b) (53). Thus, the ROI selected for a time series acquisition of intensity frames reporting eGFP-53BP1 dynamics was positioned within the nucleus, acquired under basal (−4OHT) (Fig. 6 b, left) versus DSB-induced conditions (+4OHT) (Fig. 6 c, left), and then transformed into a split brightness movie via use of the filters we defined from independent calibration of the monomeric versus multimeric brightness of eGFP (Figs. 4 a and b). As can be seen from a select set of merged eGFP-53BP1 oligomer localization maps taken from the brightness movie acquired before (Fig. 6 b, right) versus after (Fig. 6 c, right) 4OHT treatment, we find that (1) eGFP-53BP1 monomers (teal) and dimers (green) are detected throughout the nucleoplasm under basal conditions, while (2) eGFP-53BP1 higher-order oligomer formation (red) is detected upon DSB induction at nuclear locations that spatiotemporally correlate with DSB foci based on eGFP-53BP1 intensity (Figs. 6 b, c, S7 c, and d).

To investigate the spatiotemporal dynamics that underpin 53BP1 higher-order oligomer formation at DSB foci induced inside DIvA nuclei, we next performed radial pCOMB analysis at δr = 6 pixels (480 nm) on split brightness movies derived from fluorescence fluctuation data acquired before versus after 4OHT treatment. From first calculating the radial average of pCOMB6 across nuclear ROIs defined within the filtered brightness movies derived from multiple cells (N = 4) (Fig. 6 d), we find, analogous to inert eGFP oligomers (Fig. 4 f) and STAT3-eGFP
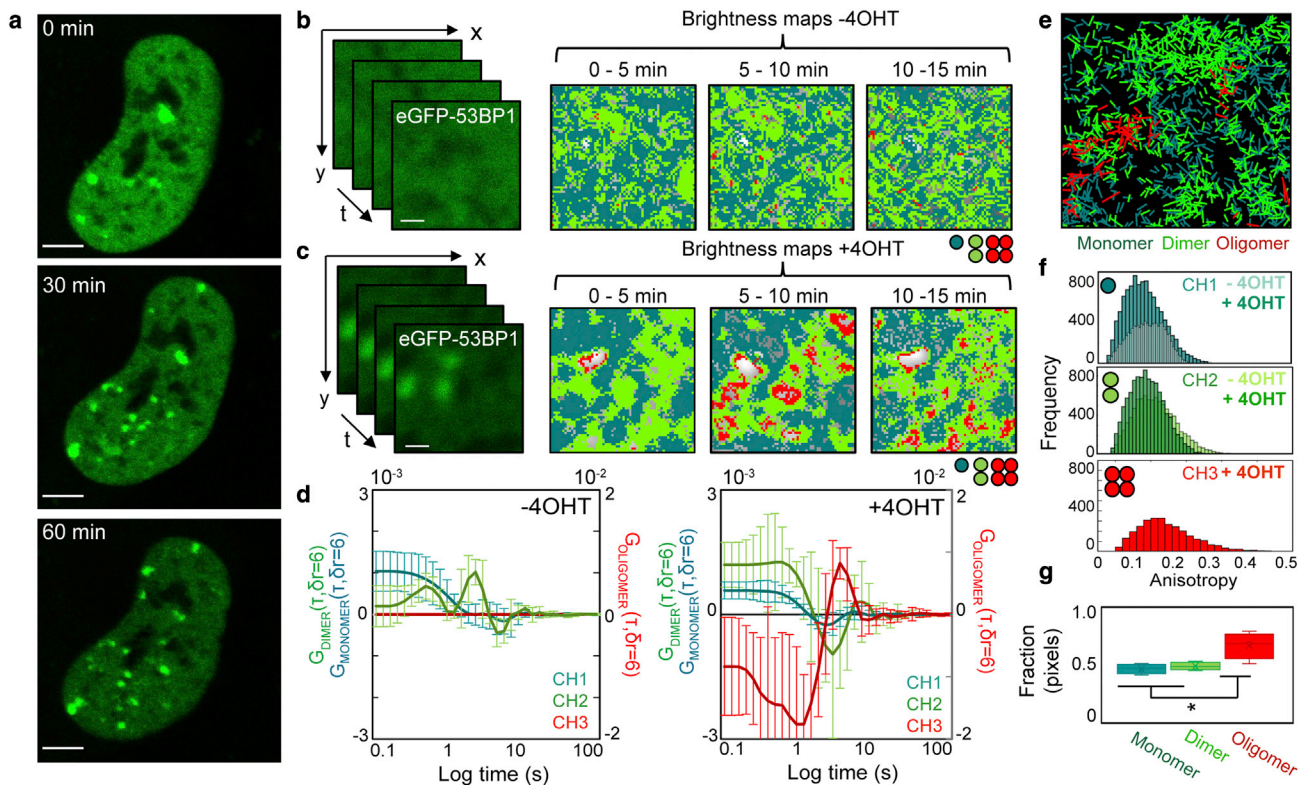
FIGURE 6   Radial pCOMB analysis of eGFP-53BP1 dimers versus oligomers in response to DNA damage. (*a*) Intensity images of DIvA cells expressing eGFP-53BP1 at t = 0 min (*top*), 30 min (*middle*), and 60 min (*bottom*) after treatment with 300 nM 4-hydroxy-tamoxifen (4OHT). Scale bar, 5 μm. (*b*) Time series of intensity frames within an ROI selected for radial pCOMB analysis prior to 4OHT treatment (*left*) and a select set of brightness frames derived from this acquisition that are weighted to record eGFP-53BP1 monomers (*teal*), dimers (*green*), and higher-order oligomers (*red*) (e.g., tetramers) (*right*). Scale bar, 1 μm. (*c*) Time series of intensity frames within an ROI selected for radial pCOMB analysis 15 min after 4OHT treatment (*left*) and a select set of brightness frames derived from this acquisition that are weighted to record eGFP-53BP1 monomers (*teal*), dimers (*green*), and higher-order oligomers (*red*) (e.g., tetramers) (*right*). Scale bar, 1 μm. (*d*) Radially averaged pCOMB profiles with standard error of the mean derived from pair correlation analysis of eGFP-53BP1 monomer, dimer, and higher-order oligomer (e.g., tetramer) transport in CH1, CH2, and CH3 of the split brightness movies derived from nuclear ROIs in DIvA cells (N = 4) before versus after 4OHT treatment across a radius of δr = 6 pixels (pCOMB6). (*e*–*f*) Merged map of connectivity (*e*) and anisotropy histograms (*f*) derived from radial pCOMB6 analysis of the split brightness movie presented in (*c*) that report where and to what extent eGFP-53BP1 monomer, dimer, and higher-order oligomer (e.g., tetramer) mobility is anisotropic before versus after 4OHT treatment. (*g*) Quantitation of anisotropy histograms constructed from radial pCOMB6 analysis of eGFP-53BP1 monomer, dimer, and higher-order oligomer (e.g., tetramer) mobility in the nucleus of DIvA cells (N = 4 DIvA). Box and whisker plot shows the minimum, maximum, sample median, and first versus third quartiles. *p < 0.05 (unpaired *t*-tests). To see this figure in color, go online.

(Fig. 5 *d*), that, under basal conditions (−4OHT), 53BP1 monomers translocate sub-micrometer nuclear distances at a significantly faster rate than 53BP1 dimers ($\tau_{\mathrm{monomer}} \sim$ 0.1 s versus $\tau_{\mathrm{dimer}} \sim$ 3.7 s). Then, interestingly, upon DSB induction (+4OHT), we found 53BP1 dimers translocate the nucleoplasm as efficiently as 53BP1 monomers (τ_{monomer} and $\tau_{\mathrm{dimer}} \sim$ 0.1 s)—an effect also transiently observed for STAT3 (Fig. 5 *d*) —simultaneous with the formation of a population of 53BP1 higher-order oligomers at DSB foci, which exhibit extremely limited mobility ($\tau_{\mathrm{oligomer}} \sim$ 6 s). Derivation of connectivity maps and construction of anisotropy histograms that report where and to what extent eGFP-53BP1 monomers, dimers, and higher-order oligomers experience anisotropic translocation upon DSB induction (Figs. 6 *e* and *f*, S7 *e* and *f*), reveals that 53BP1 monomers and dimers experience less obstruction upon DSB induction (Fig. 6 *f*), and the fraction of aniso-

tropic transits detected for each of these species across multiple nuclear connectivity maps (N = 4) (Fig. 5 *g*) is comparable with their inert eGFP counterparts (Fig. 4 *k*). Collectively, this result (Figs. 6 *d*–*g*, S7 *e* and *f*) suggests the DDR of a DSB to induce a rearrangement in nucleus architecture that promotes 53BP1 dimer surveillance and the formation of 53BP1 higher-order oligomers that exhibit DNA binding activity at DSB sites.

DISCUSSION

The biophysical mechanism by which nuclear proteins explore the multi-layered and structurally heterogeneous 3D chromatin network to arrive at a target DNA sequence remains not entirely understood (59,60). However, what is increasingly recognized is that (1) rearrangements in local chromatin compaction modulate DNA template access

([1,3,61]), (2) chromatin dynamics facilitate nuclear protein DNA target search by promoting nuclear protein accumulation at specific DNA sequences ([5–9]), and (3) several nuclear proteins scanning the genome employ self-association into different sized homo-oligomers to impart different binding affinities and specificities for the DNA template ([16,18–21]). Thus, to spatiotemporally map this complex interplay between chromatin network access and nuclear protein mobility as a function of oligomeric state, here we present a novel microscopy assay called radial pCOMB. Radial pCOMB is underpinned by a 2D pair correlation analysis of the molecular brightness fluctuations ([20,44]) that arise from a fluorescently tagged protein diffusing throughout intracellular architecture, and a moment-based analysis of the resulting spatiotemporal correlation functions ([45,46]) to enable the anisotropy of oligomer mobility to be spatially mapped. Also importantly, since this fluctuation-based method works best on a low-density population of moving particles (nanomolar), then provided a protein of interest can be labeled with a fluorophore as bright as eGFP ($\sim$25,000 cs^{-1}m^{-1}) ([52]), radial pCOMB is well suited to capture the diffusive dynamics of nuclear proteins that occur with a low copy number (e.g., TFs) ([62]).

From application of radial pCOMB to inert versus biologically active nuclear proteins, we found homo-oligomer formation to regulate the temporal kinetics of diffusion throughout the nucleoplasm and, at the same time, refine the spatial exploration volume available for DNA target search. Specifically, for eGFP multimers of increasing size, we found, in agreement with previous studies ([8,20]), that the structural framework of the nucleus represents a size-dependent hindrance to protein transport across submicrometer distances. In addition, importantly, the implication this finding has for a TF undergoing DNA target search, or a repair machine being recruited to a DNA damage site, is that (1) rearrangements in chromatin network organization can specifically regulate the diffusive properties of a subset of molecules (e.g., the dimer of STAT3 or 53BP1 during initial activation), and (2) homo-oligomer formation significantly increases obstruction (anisotropic mobility) within the nuclear landscape (e.g. the oligomer of STAT3 or 53BP1 assembled at specific nuclear locations). Thus, the arrival and retention of a nuclear protein at a target DNA template destination can be facilitated by size-based exclusion from specific nuclear compartments that are driven by chromatin network rearrangements, coupled with homo-oligomer formation within accessible nuclear compartments that likely differentially regulate DNA binding activity.

In terms of the future for radial pCOMB analysis, we envisage that this biophysical tool will be an invaluable asset for cell biologists who want to investigate protein trafficking and the impact homo-oligomer formation has on the capacity of a protein to navigate intracellular architecture ([4,13,22,63]). While we focused on DNA target search in the nucleus, importantly, radial pCOMB is amenable to probing oligomer mobility in any intracellular compartment, provided a time series of intensity frames can be acquired with sufficient spatiotemporal resolution and statistics to track the protein dynamics of interest, while maintaining a pixel dwell time that does not significantly reduce the apparent brightness of the fluorescent label that is employed. In this study, we employed a commercial laser scanning confocal microscope coupled to a photon counting detector that enabled quantitative measurement of fluorescent brightness fluctuations when 2D frame scan data were acquired with a low pixel frame size and at a high zoom. Importantly, however, radial pCOMB is, in theory, also compatible with wide-field microscopy setups based on total internal reflection fluorescence (TIRF) or a single-plane illumination microscope (SPIM) that are equipped with a fast and highly sensitive camera optimized for single-molecule biophysics ([35,64–67]). Thus, future work will be dedicated to coupling radial pCOMB with TIRF and/or SPIM so the accessibility of an entire single cell toward protein transport as a function of oligomeric state can be extracted from a large field of view and the impact protein oligomer formation has on trafficking between intracellular compartments directly uncovered.

SUPPORTING MATERIAL

Supporting material can be found online at https://doi.org/10.1016/j.bpj.2022.04.030.

AUTHOR CONTRIBUTIONS

ACKNOWLEDGMENTS

REFERENCES

1. Luger, K., M. L. Dechassa, and D. J. Tremethick. 2012. New insights into nucleosome and chromatin structure: an ordered state or a disordered affair? *Nat. Rev. Mol. Cell Biol.* 13:436–447. https://doi.org/10.1038/nrm3382.

2. Kaur, G., M. W. Costa, …, N. Plachta. 2013. Probing transcription factor diffusion dynamics in the living mammalian embryo with photoactivatable fluorescence correlation spectroscopy. *Nat. Commun.* 4:1637. https://doi.org/10.1038/ncomms2657.

3. Bonev, B., and G. Cavalli. 2016. Organization and function of the 3D genome. *Nat. Rev. Genet.* 17:661. https://doi.org/10.1038/nrg.2016.112.

4. Priest, D. G., A. Solano, …, E. Hinde. 2019. Fluorescence fluctuation spectroscopy: an invaluable microscopy tool for uncovering the biophysical rules for navigating the nuclear landscape. *Biochem. Soc. Trans.* 47:1117–1129. https://doi.org/10.1042/BST20180604.

5. Bancaud, A., S. Huet, …, J. Ellenberg. 2009. Molecular crowding affects diffusion and binding of nuclear proteins in heterochromatin and reveals the fractal organization of chromatin. *EMBO J.* 28:3785–3798. https://doi.org/10.1038/emboj.2009.340.

6. Dross, N., C. Spriet, …, J. Langowski. 2009. Mapping eGFP oligomer mobility in living cell nuclei. *PLoS One.* 4:e5041. https://doi.org/10.1371/journal.pone.0005041.

7. Hinde, E., F. Cardarelli, …, E. Gratton. 2010. In vivo pair correlation analysis of EGFP intranuclear diffusion reveals DNA-dependent molecular flow. *Proc. Natl. Acad. Sci. U S A.* 107:16560–16565. https://doi.org/10.1073/pnas.1006731107.

8. Baum, M., F. Erdel, …, K. Rippe. 2014. Retrieving the intracellular topology from multi-scale protein mobility mapping in living cells. *Nat. Commun.* 5:4494. https://doi.org/10.1038/ncomms5494.

9. Woringer, M., X. Darzacq, and I. Izeddin. 2014. Geometry of the nucleus: a perspective on gene expression regulation. *Curr. Opin. Chem. Biol.* 20:112–119. https://doi.org/10.1016/j.cbpa.2014.05.009.

10. Mirny, L., M. Slutsky, …, A. Kosmrlj. 2009. How a protein searches for its site on DNA: the mechanism of facilitated diffusion. *J. Phys. A: Math. Theor.* 42:434013. https://doi.org/10.1088/1751-8113/42/43/434013.

11. Redding, S., and E. C. Greene. 2013. How do proteins locate specific targets in DNA? *Chem. Phys. Lett.* 570:1–11. https://doi.org/10.1016/j.cplett.2013.03.035.

12. Kribelbauer, J. F., C. Rastogi, …, R. S. Mann. 2019. Low-affinity binding sites and the transcription factor specificity paradox in eukaryotes. *Annu. Rev. Cell Dev Biol.* 35:357–379. https://doi.org/10.1146/annurev-cellbio-100617-062719.

13. Funnell, A. P. W., and M. Crossley. 2012. Homo- and heterodimerization in transcriptional regulation. *Adv. Exp. Med. Biol.* 747:105–121. https://doi.org/10.1007/978-1-4614-3229-6_7.

14. Declerck, N., and C. A. Royer. 2013. Interactions in gene expression networks studied by two-photon fluorescence fluctuation spectroscopy. *Methods Enzymol.* 519:203–230. https://doi.org/10.1016/B978-0-12-405539-1.00007-5.

15. Domoszlai, T., A. Martincuks, …, G. Muller-Newen. 2014. Consequences of the disease-related L78R mutation for dimerization and activity of STAT3. *J. Cell Sci.* 127:1899–1910. https://doi.org/10.1242/jcs.137422.

16. Gaglia, G., and G. Lahav. 2014. Constant rate of p53 tetramerization in response to DNA damage controls the p53 response. *Mol. Syst. Biol.* 10:753. https://doi.org/10.15252/msb.20145168.

17. Pernus, A., and J. Langowski. 2015. Imaging Fos-Jun transcription factor mobility and interaction in live cells by single plane illumination-fluorescence cross correlation spectroscopy. *PLoS One.* 10:e0123070. https://doi.org/10.1371/journal.pone.0123070.

18. Aguilar-Arnal, L., S. Ranjit, …, P. Sassone-Corsi. 2016. Spatial dynamics of SIRT1 and the subnuclear distribution of NADH species. *Proc. Natl. Acad. Sci. U S A.* 113:12715–12720. https://doi.org/10.1073/pnas.1609227113.

19. Clark, N. M., E. Hinde, …, R. Sozzani. 2016. Tracking transcription factor mobility and interaction in Arabidopsis roots with fluorescence correlation spectroscopy. *Elife.* 5:e14770. https://doi.org/10.7554/eLife.14770.

20. Hinde, E., E. Pandzic, …, K. Gaus. 2016. Quantifying the dynamics of the oligomeric transcription factor STAT3 by pair correlation of molecular brightness. *Nat. Commun.* 7:11047. https://doi.org/10.1038/ncomms11047.

21. Presman, D. M., S. Ganguly, …, G. L. Hager. 2016. DNA binding triggers tetramerization of the glucocorticoid receptor in live cells. *Proc. Natl. Acad. Sci. U S A.* 113:8236–8241. https://doi.org/10.1073/pnas.1606774113.

22. Cammarota, E., and D. Mazza. 2019. Monitoring transcription factor oligomerization in single living cells by number and brightness analysis. *Methods Mol. Biol.* 2038:223–237. https://doi.org/10.1007/978-1-4939-9674-2_15.

23. Qian, H., and E. L. Elson. 1990. Distribution of molecular aggregation by analysis of fluctuation moments. *Proc. Natl. Acad. Sci. U S A.* 87:5479–5483. https://doi.org/10.1073/pnas.87.14.5479.

24. Qian, H., and E. L. Elson. 1990. On the analysis of high order moments of fluorescence fluctuations. *Biophys. J.* 57:375–380. https://doi.org/10.1016/S0006-3495(90)82539-X.

25. Chen, Y., L. N. Wei, and J. D. Muller. 2003. Probing protein oligomerization in living cells with fluorescence fluctuation spectroscopy. *Proc. Natl. Acad. Sci. U S A.* 100:15492–15497. https://doi.org/10.1073/pnas.2533045100.

26. Chen, Y., J. Johnson, …, J. D. Mueller. 2010. Observing protein interactions and their stoichiometry in living cells by brightness analysis of fluorescence fluctuation experiments. *Methods Enzymol.* 472:345–363. https://doi.org/10.1016/S0076-6879(10)72026-7.

27. Macdonald, P., J. Johnson, …, J. D. Mueller. 2013. Brightness analysis. *Methods Enzymol.* 518:71–98. https://doi.org/10.1016/B978-0-12-388422-0.00004-2.

28. Palmer, A. G., 3rd, and N. L. Thompson. 1987. Molecular aggregation characterized by high order autocorrelation in fluorescence correlation spectroscopy. *Biophys. J.* 52:257–270. https://doi.org/10.1016/S0006-3495(87)83213-7.

29. Muller, J. D. 2004. Cumulant analysis in fluorescence fluctuation spectroscopy. *Biophys. J.* 86:3981–3992. https://doi.org/10.1529/biophysj.103.037887.

30. Melnykov, A. V., and K. B. Hall. 2009. Revival of high-order fluorescence correlation analysis: generalized theory and biochemical applications. *J. Phys. Chem. B.* 113:15629–15638. https://doi.org/10.1021/jp906539k.

31. Digman, M. A., R. Dalal, …, E. Gratton. 2008. Mapping the number of molecules and brightness in the laser scanning microscope. *Biophys. J.* 94:2320–2332. https://doi.org/10.1529/biophysj.107.114645.

32. Digman, M. A., P. W. Wiseman, …, E. Gratton. 2009. Stoichiometry of molecular complexes at adhesions in living cells. *Proc. Natl. Acad. Sci. U S A.* 106:2170–2175. https://doi.org/10.1073/pnas.0806036106.

33. Macdonald, P. J., J. Johnson, …, J. D. Mueller. 2014. Brightness experiments. *Methods Mol. Biol.* 1076:699–718. https://doi.org/10.1007/978-1-62703-649-8_32.

34. Nolan, R., M. Iliopoulou, …, S. Padilla-Parra. 2018. Detecting protein aggregation and interaction in live cells: a guide to number and brightness. *Methods.* 140-141:172–177. https://doi.org/10.1016/j.ymeth.2017.12.001.

35. Cutrale, F., D. Rodriguez, …, S. Ojosnegros. 2019. Using enhanced number and brightness to measure protein oligomerization dynamics in live cells. *Nat. Protoc.* 14:616–638. https://doi.org/10.1038/s41596-018-0111-9.

36. Izeddin, I., V. Recamier, …, X. Darzacq. 2014. Single-molecule tracking in live cells reveals distinct target-search strategies of transcription factors in the nucleus. *Elife.* 3:e02230. https://doi.org/10.7554/eLife.02230.

37. Caccianini, L., D. Normanno, …, M. Dahan. 2015. Single molecule study of non-specific binding kinetics of LacI in mammalian cells. *Faraday Discuss.* 184:393–400. https://doi.org/10.1039/c5fd00112a.

38. Normanno, D., L. Boudarene, …, M. Dahan. 2015. Probing the target search of DNA-binding proteins in mammalian cells using TetR as model searcher. *Nat. Commun.* 6:7357. https://doi.org/10.1038/ncomms8357.

39. Liu, Z., and R. Tjian. 2018. Visualizing transcription factor dynamics in living cells. *J. Cell Biol.* 217:1181–1191. https://doi.org/10.1083/jcb.201710038.

40. Mir, M., A. Reimer, …, X. Darzacq. 2018. Single molecule imaging in live embryos using lattice light-sheet microscopy. *Methods Mol. Biol.* 1814:541–559. https://doi.org/10.1007/978-1-4939-8591-3_32.

41. Digman, M. A., and E. Gratton. 2009. Imaging barriers to diffusion by pair correlation functions. *Biophys. J.* 97:665–673. https://doi.org/10.1016/j.bpj.2009.04.048.

42. Hinde, E., M. A. Digman, …, E. Gratton. 2013. Millisecond spatiotemporal dynamics of FRET biosensors by the pair correlation function and the phasor approach to FLIM. *Proc. Natl. Acad. Sci. U S A.* 110:135–140. https://doi.org/10.1073/pnas.1211882110.

43. Mazza, D., A. Abernathy, …, J. G. McNally. 2012. A benchmark for chromatin binding measurements in live cells. *Nucleic Acids Res.* 40:e119. https://doi.org/10.1093/nar/gks701.

44. Di Rienzo, C., F. Cardarelli, …, E. Gratton. 2016. Diffusion tensor analysis by two-dimensional pair correlation of fluorescence fluctuations in cells. *Biophys. J.* 111:841–851. https://doi.org/10.1016/j.bpj.2016.07.005.

45. Malacrida, L., P. N. Hedde, …, E. Gratton. 2018. Visualization of barriers and obstacles to molecular diffusion in live cells by spatial pair-cross-correlation in two dimensions. *Biomed. Opt. Express.* 9:303–321. https://doi.org/10.1364/BOE.9.000303.

46. Hedde, P. N., E. Staaf, …, E. Gratton. 2019. Pair correlation analysis maps the dynamic two-dimensional organization of natural killer cell receptors at the synapse. *ACS Nano.* 13:14274–14282. https://doi.org/10.1021/acsnano.9b07486.

47. Levy, D. E., and I. Marie. 2012. STATus report on tetramers. *Immunity.* 36:553–555. https://doi.org/10.1016/j.immuni.2012.04.003.

48. Zhao, Y., C. Zeng, …, O. A. Timofeeva. 2013. A new role for STAT3 as a regulator of chromatin topology. *Transcription.* 4:227–231. https://doi.org/10.4161/trns.27368.

49. Zhang, X., and J. E. Darnell, Jr. 2001. Functional importance of Stat3 tetramerization in activation of the alpha 2-macroglobulin gene. *J. Biol. Chem.* 276:33576–33581. https://doi.org/10.1074/jbc.M104978200.

50. Adams, M. M., B. Wang, …, P. B. Carpenter. 2005. 53BP1 oligomerization is independent of its methylation by PRMT1. *Cell Cycle.* 4:1854–1861. https://doi.org/10.4161/cc.4.12.2282.

51. Lou, J., D. G. Priest, …, E. Hinde. 2020. Spatiotemporal dynamics of 53BP1 dimer recruitment to a DNA double strand break. *Nat. Commun.* 11:5776. https://doi.org/10.1038/s41467-020-19504-3.

52. Chen, Y., J. D. Muller, …, E. Gratton. 2002. Molecular brightness characterization of EGFP in vivo by fluorescence fluctuation spectroscopy. *Biophys. J.* 82:133–144. https://doi.org/10.1016/S0006-3495(02)75380-0.

53. Aymard, F., B. Bugler, …, G. Legube. 2014. Transcriptionally active chromatin recruits homologous recombination at DNA double-strand breaks. *Nat. Struct. Mol. Biol.* 21:366–374. https://doi.org/10.1038/nsmb.2796.

54. Iacovoni, J. S., P. Caron, …, G. Legube. 2010. High-resolution profiling of γH2AX around DNA double strand breaks in the mammalian genome. *EMBO J.* 29:1446–1457. https://doi.org/10.1038/emboj.2010.38.

55. Massip, L., P. Caron, …, G. Legube. 2010. Deciphering the chromatin landscape induced around DNA double strand breaks. *Cell Cycle.* 9:3035–3044. https://doi.org/10.4161/cc.9.15.12412.

56. Digman, M. A., C. M. Brown, …, E. Gratton. 2005. Measuring fast dynamics in solutions and cells with a laser scanning microscope. *Biophys. J.* 89:1317–1327. https://doi.org/10.1529/biophysj.105.062836.

57. Zgheib, O., K. Pataky, …, T. D. Halazonetis. 2009. An oligomerized 53BP1 tudor domain suffices for recognition of DNA double-strand breaks. *Mol. Cell Biol.* 29:1050–1058. https://doi.org/10.1128/MCB.01011-08.

58. Zimmermann, M., and T. de Lange. 2014. 53BP1: pro choice in DNA repair. *Trends Cell Biol.* 24:108–117. https://doi.org/10.1016/j.tcb.2013.09.003.

59. Singh, A. P., R. Galland, …, T. E. Saunders. 2017. 3D protein dynamics in the cell nucleus. *Biophys. J.* 112:133–142. https://doi.org/10.1016/j.bpj.2016.11.3196.

60. Woringer, M., and X. Darzacq. 2018. Protein motion in the nucleus: from anomalous diffusion to weak interactions. *Biochem. Soc. Trans.* 46:945–956. https://doi.org/10.1042/BST20170310.

61. Di Bona, M., M. A. Mancini, …, L. Lanzano. 2019. Measuring mobility in chromatin by intensity-sorted FCS. *Biophys. J.* 116:987–999. https://doi.org/10.1016/j.bpj.2019.02.003.

62. Milo, R., P. Jorgensen, …, M. Springer. 2010. BioNumbers–the database of key numbers in molecular and cell biology. *Nucleic Acids Res.* 38:D750–D753. https://doi.org/10.1093/nar/gkp889.

63. Coleman, R. A., Z. Liu, …, T. Lionnet. 2015. Imaging transcription: past, present, and future. *Cold Spring Harb Symp. Quant Biol.* 80:1–8. https://doi.org/10.1101/sqb.2015.80.027201.

64. Kolin, D. L., and P. W. Wiseman. 2007. Advances in image correlation spectroscopy: measuring number densities, aggregation states, and dynamics of fluorescently labeled macromolecules in cells. *Cell Biochem Biophys.* 49:141–164. https://doi.org/10.1007/s12013-007-9000-5.

65. Wohland, T., X. Shi, …, E. H. Stelzer. 2010. Single plane illumination fluorescence correlation spectroscopy (SPIM-FCS) probes inhomogeneous three-dimensional environments. *Opt. Express.* 18:10627–10641. https://doi.org/10.1364/OE.18.010627.

66. Bag, N., and T. Wohland. 2014. Imaging fluorescence fluctuation spectroscopy: new tools for quantitative bioimaging. *Annu. Rev. Phys. Chem.* 65:225–248. https://doi.org/10.1146/annurev-physchem-040513-103641.

67. Langowski, J. 2017. Single plane illumination microscopy as a tool for studying nucleome dynamics. *Methods.* 123:3–10. https://doi.org/10.1016/j.ymeth.2017.06.021.